



Universiteit  
Leiden  
The Netherlands

## Strategies for mechanical metamaterial design

Singh, N.

### Citation

Singh, N. (2019, April 10). *Strategies for mechanical metamaterial design*. *Casimir PhD Series*. Retrieved from <https://hdl.handle.net/1887/71234>

Version: Not Applicable (or Unknown)

License: [Leiden University Non-exclusive license](#)

Downloaded from: <https://hdl.handle.net/1887/71234>

**Note:** To cite this publication please use the final published version (if applicable).

Cover Page



Universiteit Leiden



The handle <http://hdl.handle.net/1887/71234> holds various files of this Leiden University dissertation.

**Author:** Singh, N.

**Title:** Strategies for mechanical metamaterial design

**Issue Date:** 2019-04-10

# The Soft Mechanism

---

**Abstract** – In this chapter, we show that the experimentally observed different mechanical regimes in a laterally ( $x$ -) confined *holey* elastic mechanical metamaterial [20] can qualitative be captured by a spring-coupled mechanism consisting of rotating rigid rectangles - *soft mechanism* - and discuss the physical method to do so in details. The soft mechanism allows us to understand these regimes from a geometrical perspective, extending which, we suggest a general design strategy for confinement-programmable response of mechanical metamaterials. Mainly, we propose that based on the trajectory of the mechanism, it is theoretically possible to encode plenty of other sequence of equilibria that unfold as the control parameter ( $x$ -confinement in our case) is varied. We model the inter-hole ligament in the real samples by coupling the hinges of soft mechanism with torsional springs and observe some qualitative agreements with [70] in terms of the critical values of  $x$ -confinement that separate the four successive regimes. We finally, consider the limiting case where the neighboring holes in the sample approach to be of equal size and mathematically show that these regimes result from the unfolding of an imperfect pitchfork bifurcation.



## 2.1 Introduction

We begin with presenting a brief review of the work reported in [20]. The reader is encouraged to refer to the main source for a more detailed understanding.

**Programmable mechanical metamaterials** – It has been observed both experimentally and numerically that the mechanical response of a quasi-2D elastic slab perforated with an alternating pattern of large and small equi-sized circular holes in such a manner that the center of the holes lie on a square array, called a *biholar sheet*, can be controlled by the amount of a prior external *horizontal confinement* (strain, also called *x*-confinement),  $\epsilon_x$  by means of fixed size plastic clamps. Fig. 2.1(a) shows a biholar sheet, whose geometry is set by the parameters  $D_1$ ,  $D_2$  and  $p$ , where  $D_1$ ,  $D_2$  are the respective hole diameters of the smaller and larger holes and  $p$  is the hole-separating *pitch*. We use here also the dimensionless quantities defined in the original work - *biholarity*,  $\chi$ ,

$$\chi = (D_2 - D_1)/p, \quad (2.1)$$

and minimum *thickness of the interhole ligaments*,  $t_l$ ,

$$t_l = 1 - (D_1 + D_2)/2p. \quad (2.2)$$

Fig. 2.1(b) shows a biholar sheet that is horizontally confined by using the plastic clamps. The force response ( $P$ ) to vertical compression ( $\epsilon_y$ ) can be changed from monotonic to non-monotonic to hysteretic and lastly back to monotonic again all for the same biholar sheet, when the *x*-confinement is increased. Fig. 2.2(a-d) shows, experimentally realized, the four different force-deformation responses of a biholar sheet ( $\chi = 0.30$ ,  $t_l = 0.15$ ) for different values of  $\epsilon_x$  [69]. Inside each figure, the insets show the biholar sample in its initial *x*-confined state i.e.  $\epsilon_y = 0.0$ .

**Brief explanation** – Upon compression, an *unconfined* biholar sheet undergoes a smooth pattern transformation to attain a state containing alternate mutually orthogonal ellipses. Depending upon the direction of compression, such a pattern of mutually orthogonal ellipses can exist in the following two arrangements: (*i*) the major axes of the larger ellipses are

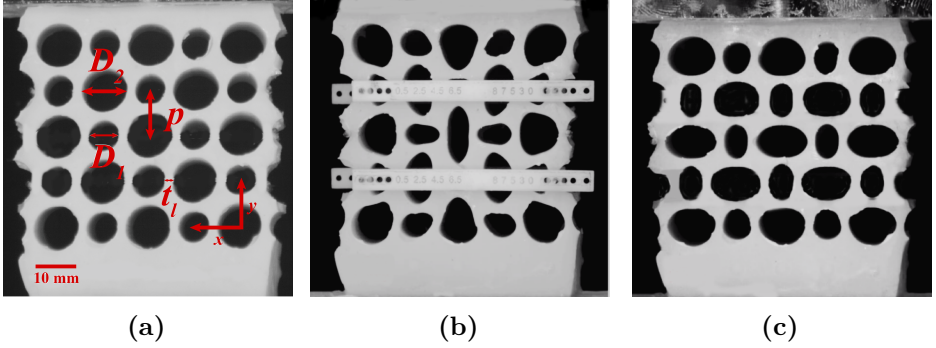


**Figure 2.1:** (a) Biholar sheet: an elastic slab perforated with an alternating pattern of large and small circular holes on a square array, characterized by the respective hole diameters  $D_1$ ,  $D_2$  of smaller and larger holes, the hole-separating *pitch* -  $p$ , and the minimum ligament thickness,  $t_l$ . Compressing the biholar sheet results in the formation of mutually orthogonal ellipses, which however, depending upon the direction of compression, can exist in two different arrangements. A biholar sheet in two differently polarized states: (b) *x-polarized* state - the sample is compressed along  $x$ -direction as a result of which the larger ellipses have their major axis oriented along the  $y$ -axis, and (c) *y-polarized* state - the sample is compressed along the  $y$ -direction, which leads to the larger ellipses orient their major axis parallel to the  $x$ -direction. These images are adopted from [69].

oriented parallel to the  $y$ -direction. This happens when the biholar sheet is compressed along the  $x$ -direction, and likewise (ii) the major axes of the larger ellipses are oriented along to the  $x$ -direction. This happens when the biholar sheet is compressed along the  $y$ -direction. The difference in the hole sizes breaks the  $90^\circ$  rotational symmetry that is present when the holes are of equal size. This causes a difference in the polarization of the hole pattern, depending along which direction the sample is compressed. In the original work, these two differently *polarized* states are referred to as *x-polarized* and *y-polarized* states respectively and are shown in Fig. 2.1(b,c).

It can be imagined that the application of an initial  $x$ -confinement followed by a subsequent vertical compression can lead to a pattern switch from a  $x$ -polarized state to a  $y$ -polarized state. Depending upon the magnitude of the  $x$ -confinement, such a pattern switch can be both smooth or discontinuous. As a result of the symmetry breaking, the deformations along

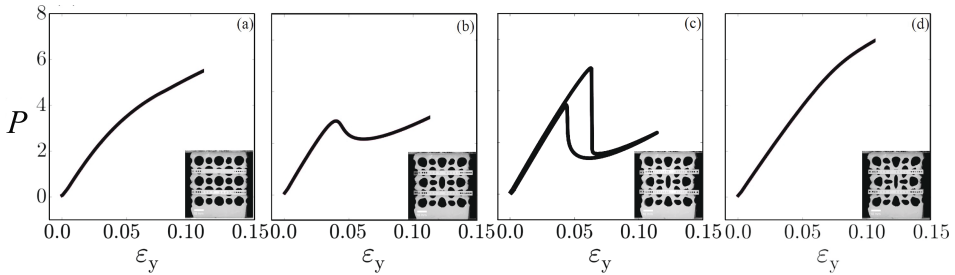


**Figure 2.2:** Experimentally observed mechanical response of a  $x$ -confined  $5 \times 5$  biholar sheet with geometrical parameters  $D_1 = 7$  mm,  $D_2 = 10$  mm,  $t_l = 0.15$ .  $\epsilon_x$  denotes the  $x$ -confinement. (a)  $\epsilon_x = 0.0$ ,  $P(\epsilon_y)$  is monotonic. (b)  $\epsilon_x = 0.12$ ,  $P(\epsilon_y)$  is non-monotonic. (c)  $\epsilon_x = 0.15$ ,  $P(\epsilon_y)$  is hysteretic. (d)  $\epsilon_x = 0.18$ ,  $P(\epsilon_y)$  is monotonic. The insets within the figures show the initial state of the confined biholar sheet i.e. at  $\epsilon_y = 0.0$ . The figures are adopted from [69].

the two primary axes interact nonlinearly. Indeed, this nonlinear coupling between the  $x$ - and the  $y$ -polarized states set up by the interacting forces of horizontal confinement and vertical compression results in the nontrivial mechanics of a confined biholar sheet [Fig. 2.2].

In this chapter, we first show that the experimentally realized mechanics of a confined biholar sheet can qualitatively be captured by a spring coupled one-degree-of-freedom mechanism consisting of pin-jointed rectangles. We call this the *soft mechanism*. We discuss in details the physical method to model the experiments in §2.2. We employ the mechanism to understand the different mechanical regimes from a geometrical perspective and based on which, we layout a general design strategy in §2.3, following which, plenty of other sequences of equilibria can be constructed leading to diverse confinement controlled responses. We take into account the thickness of the hole-connector ligaments by coupling the hinges of the mechanism with torsional springs in §2.4. Finally in §2.5, we explore the mechanism for the limiting case where the neighboring holes become ‘almost’ equi-sized,  $\chi \rightarrow 0$ , and mathematically show that the different regimes emerge from the unfolding of a pitchfork bifurcation.

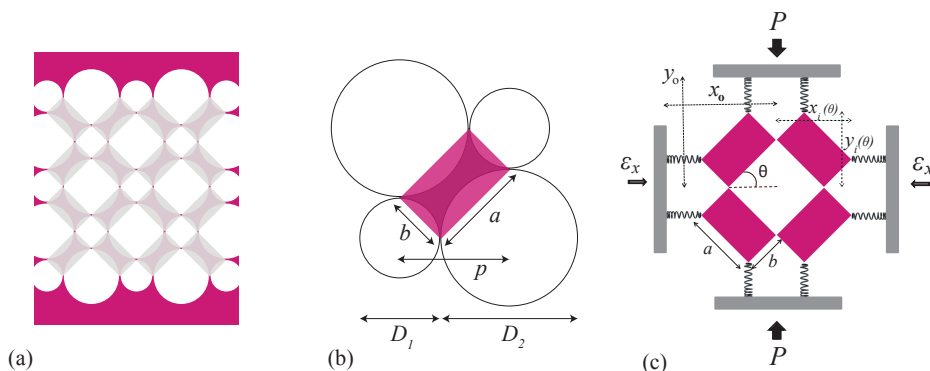


**Figure 2.3:** Soft mechanism - a mechanical model that is aimed to qualitatively capture the mechanical response of an  $x$ -confined biholar sheet [Fig. 2.2]. (a) In a biholar sheet with thin interhole ligaments, the deformations primarily occur via the bending of the ligaments and can be approximated by a mechanism consisting of pin-jointed, rigid rectangles. (b) The mapping between the rectangular rigid unit of the mechanism and the elastic unit of a biholar sheet. (c) Soft mechanism - spring coupled representative unit of the full mechanism shown in (a). The enclosing walls model the lateral confinement ( $\epsilon_x$ ) and vertical strain ( $\epsilon_y$ ).

## 2.2 Soft Mechanism Model

In this section, we derive a simple geometry-based model that captures important aspects of the mechanics of a confined biholar sheet, based on [20].

**Soft mechanism** – The deformations in a biholar sheet with vanishingly small thickness of the interhole ligaments (denoted by  $t_l$  in Fig. 2.1(a)) occur primarily via the bending of these ligaments. In such a case, the deformation of the elastic units is minimal, and thus the process can be modeled via an equivalent one-degree-of-freedom mechanism consisting of pin-jointed rigid rectangles [Fig. 2.3(a)]. The mapping of these rectangular units of length  $a$  and width  $b$  onto the elastic units is shown in Fig. 2.3(b). One unit cell of such a mechanism is sufficient for our purpose [Fig. 2.3(c)], which we use to capture the mechanical response. To incorporate the storage of the elastic energy into the system, the free corners of the rectangular units are coupled to the enclosing walls both horizontally and vertically

by a set of four linear springs. The enclosing horizontal and vertical walls model the lateral confinement ( $\epsilon_x$ ) and the vertical strain ( $\epsilon_y$ ), respectively.

**Biholarity** – With the mapping shown in Fig. 2.3(b), we express the dimensionless biholarity [Eq. (2.1)] in terms of  $a$  and  $b$ . We note that  $D_1 = b\sqrt{2}$ ,  $D_2 = a\sqrt{2}$  and  $p = (a + b)/\sqrt{2}$ . Substituting these values in Eq. (2.1) gives:

$$\chi = 2 \frac{(a - b)}{(a + b)}. \quad (2.3)$$

In the remainder of the work, we choose our lengths so that  $a + b = \sqrt{2}$ . Therefore,

$$\chi = \sqrt{2}(a - b). \quad (2.4)$$

For simplicity, considering  $a \geq b$  ( $a$  and  $b$  are interchangeable), the allowed range of biholarity is  $\chi \in [0, 2]$ .

### 2.2.1 Load-Deformation Response

We mathematically model the displacement controlled loading of a biholar sheet by following a quasi-static deformation approach for the soft mechanism. We begin with the total internal energy stored inside the soft mechanism,  $U$ , under the influences of the external  $x$ -confinement,  $\epsilon_x$ , and the vertical load,  $P$ . The total internal energy  $U$  is given by

$$U = E_x + E_y, \quad (2.5)$$

where  $E_x$  and  $E_y$  are the total elastic energies stored in the horizontal and vertical springs respectively. A quasi-static approach implies that at any given instant, the system is in equilibrium. Hence,  $E_y$  in the above equation can be replaced by the work done on the system by the acting load  $P$ . We denote it with  $W$ . Therefore, Eq. (2.5) becomes

$$U = E_x + W. \quad (2.6)$$

We know that since the soft mechanism contains only one internal degree-of-freedom, its state can completely be parameterized in terms of one variable. We use  $\theta$  for this purpose [Fig. 2.3(c)]. In effect,  $\theta = \pi/4$  represents the neutral state of the biholar sheet, whereas,  $\theta > \pi/4$  and  $\theta < \pi/4$  represent the  $x$ -polarized and  $y$ -polarized states respectively [Fig.

2.1(b,c)]. In terms of  $\theta$ , we define two more quantities:  $x_i(\theta)$  and  $y_i(\theta)$ , which denote the maximum  $x$  and  $y$  dimensions of the rectangular unit of the mechanism. With the length  $a$  and the width  $b$  of the rectangular unit,  $x_i(\theta)$  and  $y_i(\theta)$  can be expressed as:

$$x_i(\theta) = a \cos \theta + b \sin \theta, \quad (2.7)$$

and,

$$y_i(\theta) = a \sin \theta + b \cos \theta. \quad (2.8)$$

Let us suppose that upon the application of some initial  $x$ -confinement,  $\epsilon_x$ , the soft mechanism changes from its *neutral state* at  $\theta = \pi/4$  to some other state given by  $\theta$ .  $E_x$  at this perturbed state can be expressed as

$$\begin{aligned} E_x &= 4 \times \frac{1}{2} k_x \left( \epsilon_x + x_i(\theta) - x_i \left( \frac{\pi}{4} \right) \right)^2, \\ &= 2k_x \left( \epsilon_x + x_i(\theta) - x_i \left( \frac{\pi}{4} \right) \right)^2, \\ &= 2k_x (\epsilon_x + x_i(\theta) - 1)^2, \quad (\text{because } x_i(\pi/4) = 1), \end{aligned} \quad (2.9)$$

where  $k_x$  is the spring constant of the horizontal springs. The term inside the parentheses of the above equation denotes the net compression or extension of the horizontal springs<sup>1</sup>.  $\epsilon_x$  is positive for compression and negative for extension.

The total work done on the system,  $W$  can be written as

$$\begin{aligned} W &= 2P \left( y_i(\theta) - y_i \left( \frac{\pi}{4} \right) \right), \\ &= 2P(y_i(\theta) - 1), \quad (\text{because } y_i(\pi/4) = 1). \end{aligned} \quad (2.10)$$

Substituting the values of  $E_x$  and  $W$  respectively from the Eq. (2.9) and Eq. (2.10) into Eq. (2.6) (along with utilizing the expressions for  $x_i(\theta)$  and  $y_i(\theta)$  from Eq. (2.7) and Eq. (2.8)), an expression of  $U$  in terms of  $\theta$  can be obtained. Since the equilibrium state of the mechanism is changed to

<sup>1</sup>Let us assume that  $L$  denotes the rest length of the horizontal springs [Fig. 2.3(c)]. Then,  $L + x_i(\pi/4) = x_o$ . If the application of the horizontal strain  $\epsilon_x$  changes the length of the spring to  $L'$ , one can then write  $\epsilon_x + L' + x_i(\theta) = x_o$ .  $\epsilon_x$  is positive for compression and negative for extension. Therefore, change in the length of the springs  $|L - L'| = \epsilon_x + x_i(\theta) - x_i(\pi/4) = \epsilon_x + x_i(\theta) - 1$ .

another adjacent equilibrium state in response to the change in the vertical load  $P$ , then in order to maintain that, the condition of  $\partial U/\partial\theta = 0$  must be met. Setting up this condition leads to an equation relating  $P$  with the other variables:

$$P = -2k_x(\epsilon_x + x_i(\theta) - 1) \left( \frac{-a \sin \theta + b \cos \theta}{a \cos \theta - b \sin \theta} \right). \quad (2.11)$$

The vertical strain  $\epsilon_y$  can be expressed as

$$\epsilon_y = (1 - y_i(\theta)) + \frac{P}{2k_y}, \quad (2.12)$$

where  $k_y$  is the spring constant of the vertical springs. In Eq. (2.12),  $(1 - y_i(\theta))$  is the vertical deformation in the mechanism apart from the compression in the springs and  $P/2k_y$  is the compression in the springs (because the load is always quasi-statically balanced by the spring force).

For fixed  $a$ ,  $b$  and  $\epsilon_x$ , Eq. (2.11) and Eq. (2.12) together with Eq. (2.7) and Eq. (2.8) establish explicit functions of  $\theta$  to  $P$  and  $\epsilon_y$ , and hence provide an implicit relationship between the load,  $P$  and the vertical strain,  $\epsilon_y$ . Given the values of  $a$ ,  $b$  (i.e. the biholarity  $\chi$ , Eq. 2.4) and  $\epsilon_x$ , and the values of the spring constants,  $k_x$  and  $k_y$ , one can implicitly obtain the load-deformation curve,  $P(\epsilon_y)$ . Numerically, this is done by varying the value of  $\theta$  from 0 to  $\pi/2$  and separately calculating the values of  $P$  and  $\epsilon_y$  from Eq. (2.11) and Eq. (2.12) respectively, thereby obtaining a discretized version of the  $P(\epsilon_y)$  curve.

**Load-deformation curves** – We now utilize the derived Eq. (2.11) and Eq. (2.12) and show  $P(\epsilon_y)$  for a system with  $\chi = 0.30$  ( $a \approx 0.81$  and  $b \approx 0.60$ )<sup>2</sup>. We use the same value for the two spring constants :  $k_x, k_y = 0.50$ . For four different values of  $\epsilon_x$ ,  $P(\epsilon_y)$  is shown in the Fig. 2.4(a-d). Each figure displays a different qualitative trend, which we refer to as regimes (*i-iv*)<sup>3</sup>. Below we discuss them separately :

---

<sup>2</sup>Unless otherwise mentioned, we keep the value of  $\chi$  fixed to 0.30 in the rest of the chapter as well.

<sup>3</sup>For now only the *primary branches* (shown in black) in Fig. 2.4 are relevant. In §2.3.1, we describe the emergence of the secondary red branches in detail. By the primary branch we mean the solution branch which connects to the unique solution branch that exists for  $\epsilon_y \ll 0$ .

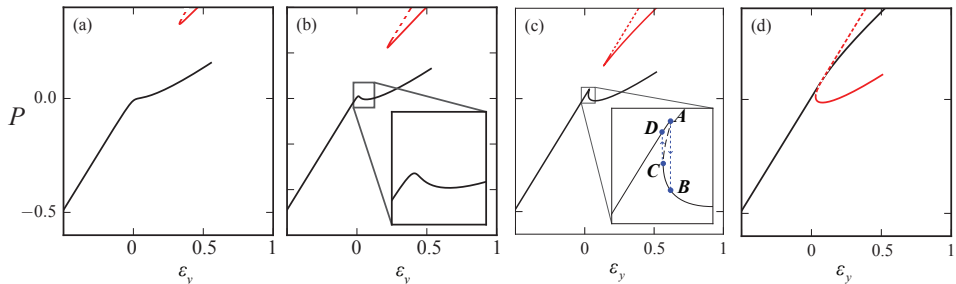


**Figure 2.4:**  $P(\epsilon_y)$  for a system with  $\chi = 0.30$  ( $a \approx 0.81$  and  $b \approx 0.60$ ). Within each figure, the primary branch (of current relevance) is shown in black and the secondary branch is shown in red (discussed in §2.3.1), and on these branches, the stable and the unstable equilibria are shown in the solid and the dashed curves respectively. **(a)**  $\epsilon_x = -0.015$ ,  $P(\epsilon_y)$  increases monotonically. **(b)**  $\epsilon_x = 0.010$ ,  $P(\epsilon_y)$  is non-monotonic. **(c)**  $\epsilon_x = 0.028$ ,  $P(\epsilon_y)$  exhibits hysteresis. Hysteretic jumps are shown in the inset with  $A - B$  and  $C - D$  jumps corresponding to the loading and the unloading deformation paths respectively. We discuss this more clearly in the text. **(d)**  $\epsilon_x = 0.040$ ,  $P(\epsilon_y)$  becomes monotonic again. With these four regimes, the soft-mechanism successfully models the experimentally observed mechanical response [Fig. 2.2]. Unlabeled axis ticks and tick labels are shared.

**Regime (i):** For  $\epsilon_x = -0.015$  [Fig. 2.4(a)], the  $P(\epsilon_y)$  curve increases monotonically with  $\epsilon_y$ . However, the slope of the curve varies. The initial value of slope = 0.50, which is equal to  $k_y$ . This is true for all the four regimes **(i)**-**(iv)**. The slope of the curve then decreases, and finally increases again. The mechanism behaves as a nonlinear elastic material in this regime.

**Regime (ii):** For  $\epsilon_x = 0.010$  [Fig. 2.4(b)], the  $P(\epsilon_y)$  curve becomes non-monotonic; displaying a *dip*. As we will show in §2.3.1, the dip in the  $P(\epsilon_y)$  curve results from a polarization change<sup>4</sup>. Positive value of  $\epsilon_x$  makes the mechanism  $x$ -polarized [Fig. 2.2(b) inset]. The polarization changes to  $y$ -polarized state under the influence of  $P$ .

<sup>4</sup>Here, and while discussing the regimes **(iii)**, **(iv)** in the following discussion, we very briefly mention the related polarization states and switches. We discuss them in details in §2.3.1.

**Regime (iii):** For  $\epsilon_x = 0.028$  [Fig. 2.4(c)], the  $P(\epsilon_y)$  curve is clearly non-monotonic but different from the one in Fig. 2.4(b). The formation of a cusp and multi-valuedness of  $P(\epsilon_y)$  signals hysteresis with characteristic hysteretic jumps (see inset). During loading the mechanism follows the path that includes a *jump* from  $\mathbf{A} - \mathbf{B}$ , while during unloading the mechanism follows another path that includes a jump from  $\mathbf{C} - \mathbf{D}$ . This also makes the path  $\mathbf{A} - \mathbf{C}$  unstable and thus is shown as a dashed curve. From a polarization point of view, these jumps result from a *sudden* polarization switch:  $x$  to  $y$  polarization switch during  $\mathbf{A} - \mathbf{B}$  jump and  $y$  to  $x$  polarization switch during  $\mathbf{C} - \mathbf{D}$  jump. Quick jumps from one polarization state to another at a fixed  $\epsilon_x, \epsilon_y$  demonstrates bistability. In the experiments these jumps are associated with *snap-through buckling* [71].

**Regime (iv):** For  $\epsilon_x = 0.040$  [Fig. 2.4(d)], the  $P(\epsilon_y)$  curve becomes monotonic again. This is however not the same as in regime (i), but is indeed exactly opposite from a polarization perspective - the previously secondary branch is now primary and vice-versa. High values of  $\epsilon_x$  makes the sample *strongly*  $x$ -polarized (see biholar sample in Fig. 2.2(d), inset) which gets further accentuated with the application of the load.

A qualitative match with the experimental and finite element simulation results shown in the original work confirms the robustness of the soft mechanism to model the mechanical response of a laterally confined biholar sheet. We point out that the above discussed regimes (i)-(iv) exist for a range of  $\epsilon_x$ . The switch from one regime to another (which may or may not involve a bifurcation<sup>5</sup>), however, occurs at fixed critical values of  $\epsilon_x$ . If given that  $k_x$  and  $k_y$  have the same values, both the range and the critical values of  $\epsilon_x$  demarcating the four regimes depends on the value of  $\chi$ . We derive the general analytical expressions for these critical strain values in the next section.

## 2.2.2 Internal Energy of the System

We will now have a closer look at the energy curves. Using Eq. (2.5), the total elastic energy,  $U$  is equal to  $E_x + E_y$ . The expression for  $E_x$  is given

<sup>5</sup>This depends on whether there are some equilibrium points whose stability has been altered or not.

by Eq. (2.9), and below the expression for  $E_y$  is provided:

$$\begin{aligned}
 E_y &= 2 \times 2 \times \frac{1}{2} \times k_y \left( \frac{P}{2k_y} \right)^2, \\
 &= \frac{P^2}{2k_y}.
 \end{aligned} \tag{2.13}$$

Therefore,

$$U = 2k_x (\epsilon_x + x_i(\theta) - 1)^2 + \frac{P^2}{2k_y}. \tag{2.14}$$

**Energy curves** – Utilizing Eq. (2.14) and Eq. (2.12), one can numerically obtain the  $U(\epsilon_y)$  curves for a system with given  $\chi$  and  $\epsilon_x$ . We now discuss  $U(\epsilon_y)$  for the same system and the same four values of  $\epsilon_x$  as in Fig. 2.4(a-d). The results are shown in Fig. 2.5(a-d). Within each figure, we show the primary branch (black) in the main panel and both the primary and secondary (red) branches in the inset panel. We focus on the primary branches to characterize the regimes:

**Regime (i):** For  $\epsilon_x = -0.015$  [Fig. 2.5(a)], the  $U(\epsilon_y)$  curve has one global minimum ( $U = 0.0$ ), which occurs for the value of  $\epsilon_y$  when  $P = 0$  because  $P = \Delta U / \Delta \epsilon_y$ . As we can clearly notice from the inset that the primary and the secondary branches are well-separated, making the later ‘infeasible’.

**Regime (ii):** For  $\epsilon_x = 0.010$  [Fig. 2.5(b)], the  $U(\epsilon_y)$  curve consists of two global minima separated by a shallow maximum -  $P(\epsilon_y)$  is non-monotonic

**Regime (iii):** For  $\epsilon_x = 0.028$  [Fig. 2.5(c)], the  $U(\epsilon_y)$  provides another perspective to the hysteresis and the associated bistability. The labeled points **A**, **B**, **C** and **D** in the inset correspond to the same points previously shown in Fig. 2.4(c). The paths **DAB** and **BCD** correspond to the loading and unloading respectively. Hysteretic jumps occur from **A** – **B** during loading and from **C** – **D** during unloading. The path **A** – **C** is unstable and is therefore shown in a dashed curve.

**Regime (iv):** For  $\epsilon_x = 0.040$  [Fig. 2.5(d)], the  $U(\epsilon_y)$  once again has only one global minimum -  $P(\epsilon_y)$  is monotonic. In the inset, we notice that

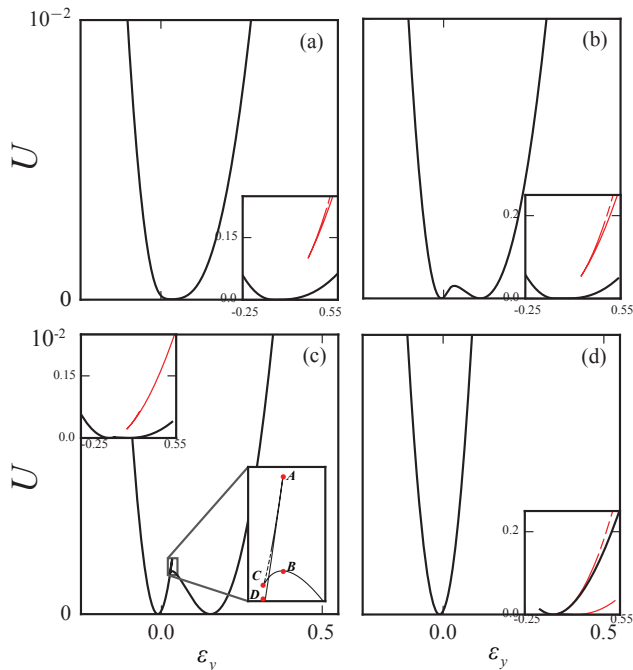


**Figure 2.5:**  $U(\epsilon_y)$  for a system with  $\chi = 0.30$  ( $a \approx 0.81$  and  $b \approx 0.60$ ), and for the same four values of  $\epsilon_x$  as shown in Fig. 2.4(a-d). Within each figure, the primary branch (of current relevance) is shown in black (main panel) and the secondary branch is shown in red (inset panel), and the stable and the unstable equilibria are shown in the solid and dashed curves respectively. (a)  $\epsilon_x = -0.015$ ,  $U(\epsilon_y)$  consists of only one global minimum. (b)  $\epsilon_x = 0.010$ ,  $U(\epsilon_y)$  consists of two local minima separated by a local maximum. (c)  $\epsilon_x = 0.028$ ,  $U(\epsilon_y)$  exhibits hysteresis. The labeled points **A**, **B**, **C**, **D** are the same as in Fig. 2.4(c). (d)  $\epsilon_x = 0.040$ ,  $U(\epsilon_y)$  consists of a global minimum. Because,  $P = \Delta U / \Delta \epsilon_y$ ,  $P(\epsilon_y)$ , we can verify that the figures (a)-(d) correspond to the regimes **(i)**-**(iv)**.

the primary and the secondary branches intersect. The system however does not switch from one state branch to another. As we will show in the next section: two values of  $\theta$  can exist for a single value of  $\epsilon_y$  for this case. So, although, when extracted numerically, the primary and the secondary branches intersect on a  $U(\epsilon_y)$  graph, they are separated in the  $\theta(\epsilon_y)$  graph; and the system only follows the primary branch of  $\theta$ .

## 2.3 Geometrical Interpretation

For fixed biholarity  $\chi$ , we have essentially two control parameters: the horizontal confinement,  $\epsilon_x$  and the vertical strain,  $\epsilon_y$ . The values of these control parameters dictate the number of possible equilibria and their stability. In this section, we introduce a geometrical interpretation of the model, through which we gain new insights about equilibria and their stability. Based on such an interpretation, we ultimately demonstrate a novel geometrical interpretation of the previously described regimes *(i)*-*(iv)*. Simultaneously, we also explain the existence of the primary and the secondary solution branches and the stable and unstable equilibria that constitute them. We conclude this section by suggesting an inverse strategy to programme other new confinement controlled responses in mechanical metamaterials whose deformations can be modeled by one-degree-of-freedom mechanisms. We propose that based on the trajectory of the mechanism, we can encode plenty of other equilibria sequence that unfold as the control parameter  $\epsilon_x$  is varied.

We begin with deriving a convenient expression for the total elastic energy stored in the system  $U$ . We reuse the expression for the elastic energy stored in the horizontal springs,  $E_x$  from Eq. (2.9). Setting  $k_x = 0.50$ , we get

$$E_x = (x_i(\theta) - (1 - \epsilon_x))^2. \quad (2.15)$$

We define a new quantity:  $X_o = 1 - \epsilon_x$ . The above equation now becomes:

$$E_x = (x_i(\theta) - X_o)^2. \quad (2.16)$$

In a corresponding manner, we can write down the elastic energy stored in the vertical springs,  $E_y$  as:

$$E_y = (y_i(\theta) - Y_o)^2, \quad (2.17)$$

where  $Y_o = 1 - \epsilon_y$ . Adding together the Eq. (2.16) and Eq. (2.17), we obtain a new expression for  $U$ :

$$U = (x_i(\theta) - X_o)^2 + (y_i(\theta) - Y_o)^2. \quad (2.18)$$

**M curve** – The dependence of the internal coordinates  $x_i$  and  $y_i$  on  $\theta$  are given by Eq. (2.7) and Eq. (2.8) respectively. In the  $(x, y)$  plane, the

locations of  $x_i$  and  $y_i$  as function of  $\theta$  trace out an elliptical curve oriented at an angle  $\pi/4$  with respect to the positive  $x$ -axis, but, for the relevant range  $0 \leq \theta \leq \pi/2$ , only a part of it. We refer to the curve relating  $x_i$  and  $y_i$  as  $\mathbf{M}$  curve ( $\mathbf{M}$  for mechanism). The eccentricity of this ellipse depends on the values of  $a$  and  $b$  and hence  $\chi$ . The ellipse *approaches* a straight line ( $x_i(\theta) = y_i(\theta)$ ) for  $\chi \rightarrow 0$  and a circle ( $x_i(\theta)^2 + y_i(\theta)^2 = \sqrt{2}$ ) for  $\chi \rightarrow 2$ . For  $\chi = 0.30$  ( $a \approx 0.81$  and  $b \approx 0.60$ ),  $\mathbf{M}$  is shown in pink in Fig. 2.6(b).

**Equi-energy circles** – Eq. (2.18) implies that the equilibrium state(s) for fixed  $(X_o, Y_o)$  are given by the extrema of  $U(\theta)$ . These equilibrium state(s) determine the state of the soft mechanism. It is possible to extract these equilibria geometrically as follows: curves of equal energy in the  $(x, y)$  plane are circles with their center at  $(X_o, Y_o)$  and radius  $\sqrt{U}$ . With the center at  $(X_o, Y_o)$ , the intersections of these circles with  $\mathbf{M}$  form an *energy landscape*:  $U(\theta)$ , the extrema of which correspond to the equilibrium states of the mechanism. Through four different constructions, we will now cover some unique scenarios for fixed  $(X_o, Y_o)$ . Mainly, these constructions will be helpful for the forthcoming discussion.

Fig. 2.6(a) shows examples of two concentric *equi-energy* circles originating from the center  $(X_o, Y_o)$ . The circle  $\mathbf{C}_1$ , shown in blue, is a tangent to  $\mathbf{M}$ , *touching* it at  $M_1$ , whereas the circle  $\mathbf{C}_2$  (in red) with slightly larger radius, intersects  $\mathbf{M}$  at two distinct points  $M_2$  and  $M_3$ , which lie on the opposite sides of  $M_1$ . Circles intersecting  $\mathbf{M}$  at the immediate vicinity of  $M_1$  have larger radii than  $\mathbf{C}_1$  and thus higher  $U$ . The local  $U(\theta)$  landscape for the given  $(X_o, Y_o)$  has therefore a minimum at the value of  $\theta_{M_1}$ , resulting in a stable equilibrium state.

Such constructions also find unstable equilibria. In Fig. 2.6(b), the positioning of the point  $(X_o, Y_o)$  allows to draw three tangential circles  $\mathbf{C}_1, \mathbf{C}_2, \mathbf{C}_3$  to  $\mathbf{M}$ , shown in the color blue, green and red respectively. These circles intersect  $\mathbf{M}$  at  $M_1, M_2$  and  $M_3$ .  $\theta_{M_1}, \theta_{M_2}$  corresponds to stable equilibrium states. The explanation is the same as earlier: the energy along the  $\mathbf{M}$  increases away from the points of tangency. The case for  $M_3$  is however opposite. Circles with slightly smaller radii than  $\mathbf{C}_3$  can intersect  $\mathbf{M}$  (at two distinct points) in the vicinity of  $M_3$ . The local  $U(\theta)$  landscape has a maximum and hence  $\theta_{M_3}$  corresponds to an unstable equilibrium configuration. Consistent with Fig. 2.6(b), we will, in the future, show the tangential circles for unstable states in dashed and solid for the stable

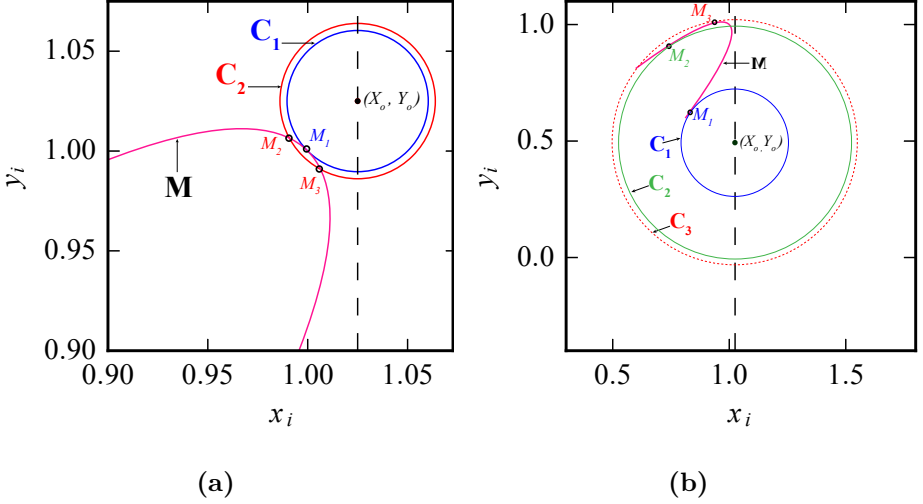


**Figure 2.6:** Given a fixed  $(X_o, Y_o)$ , the equilibrium states (and their stability) of the soft mechanism can be geometrically determined by drawing tangential circles [Eq. (2.18)]. Positioning of the point  $(X_o, Y_o)$  can lead to different scenarios. (a) Circle  $\mathbf{C}_1$ , shown in blue, centered at  $(X_o, Y_o)$  touches  $\mathbf{M}$  (in pink) at  $M_1$ . The internal energy  $U$  increases for a slightly larger circle  $\mathbf{C}_2$  (in red) that intersects  $\mathbf{M}$  at  $M_2$  and  $M_3$ . The local  $U(\theta)$  landscape has a local minimum at  $\theta$  corresponding to  $M_1$ ;  $\theta_{M_1}$  corresponds to a stable equilibrium point. (b) From  $(X_o, Y_o)$ , three tangential circles  $\mathbf{C}_1, \mathbf{C}_2, \mathbf{C}_3$  to  $\mathbf{M}$  (shown in blue, green and red respectively) can be constructed. These circles intersect  $\mathbf{M}$  at  $M_1, M_2, M_3$  respectively. With the same argument as in (a), it can be shown that  $\theta_{M_1}$  and  $\theta_{M_2}$  correspond to stable equilibrium points.  $\theta_{M_3}$  however corresponds to an unstable solution; it is possible to construct circles with slightly smaller radii than  $\mathbf{C}_3$  that intersect  $\mathbf{M}$  at two distinct points in the immediate vicinity of  $M_3$ . The local  $U(\theta)$  landscape thus has a maximum at  $\theta_{M_3}$ .

states.

We now demonstrate two cases where the point  $(X_o, Y_o)$  is inside  $\mathbf{M}$ .  $(X_o, Y_o)$  in Fig. 2.7(a) is 'contained within' the cusp of the *evolute*  $\Sigma$  (in black). The evolute of a curve is the locus of all its centers of curvature. The  $x$  and  $y$  coordinates of  $\Sigma$ ,  $x_e, y_e$  can be expressed in terms of  $\theta$  by the

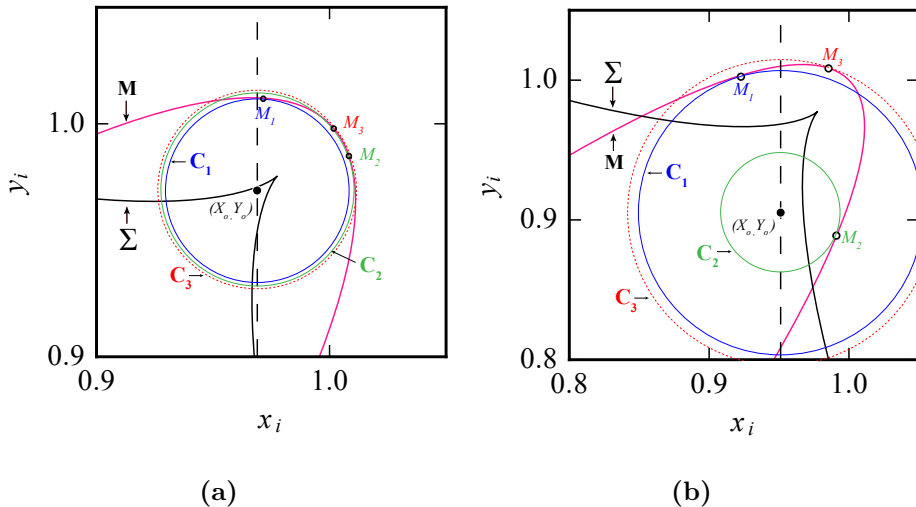


**Figure 2.7:** Given a fixed  $(X_o, Y_o)$ , the equilibrium states (and their stability) of the soft mechanism can be geometrically determined in terms of  $\theta$  by drawing tangential circles [Eq. (2.18)]. We demonstrate it for two different constructions where the point  $(X_o, Y_o)$  is ‘inside’  $\mathbf{M}$  (in pink). (a)  $(X_o, Y_o)$  is *contained within* the cusp of evolute of  $\mathbf{M}$ ,  $\Sigma$  (in black). Three concentric circles -  $\mathbf{C}_1, \mathbf{C}_2, \mathbf{C}_3$  (colored blue, green and red) can be constructed from  $(X_o, Y_o)$  that are tangential  $\mathbf{M}$ .  $\mathbf{C}_1, \mathbf{C}_2, \mathbf{C}_3$  touch  $\mathbf{M}$  at  $M_1, M_2$  and  $M_3$  respectively.  $M_1$  and  $M_2$  correspond to stable equilibrium solutions.  $M_3$  however corresponds to an unstable equilibrium solution. This is true for any point on the dashed vertical line that is *contained within*  $\Sigma$ . (b) The three tangential circles  $\mathbf{C}_1, \mathbf{C}_2, \mathbf{C}_3$  (colored blue, green and red) touch  $\mathbf{M}$  at  $M_1, M_2$  and  $M_3$  respectively. Solutions are stable at  $M_1, M_2$  and unstable at  $M_3$ .

following parametric equations:

$$x_e = x_i(\theta) - \frac{(a \cos \theta - b \sin \theta)(a^2 + b^2 - 2ab \sin 2\theta)}{a^2 - b^2}, \quad (2.19)$$

$$y_e = y_i(\theta) - \frac{(a \sin \theta - b \cos \theta)(a^2 + b^2 - 2ab \sin 2\theta)}{a^2 - b^2}. \quad (2.20)$$

Centered at  $(X_o, Y_o)$ , it is possible to draw three tangential circles  $\mathbf{C}_1, \mathbf{C}_2, \mathbf{C}_3$  (colored blue, green and red respectively) to  $\mathbf{M}$  that form

tangencies at the points  $M_1, M_2, M_3$ .  $\theta_{M_1}, \theta_{M_2}$  correspond to stable solutions whereas  $\theta_{M_3}$  corresponds to an unstable solution. Similarly, the existence of two stable and one unstable equilibrium solution can be proved for any point on the dashed line in Fig. 2.7(a) that is contained within  $\Sigma$ . We will later encounter this case again when we discuss the geometrical interpretation of the regime *(iii)*.

Fig. 2.7(b) shows the fourth and last example. We construct the three tangential circles  $\mathbf{C}_1, \mathbf{C}_2, \mathbf{C}_3$  (colored blue, green and red respectively) to  $\mathbf{M}$ . These circles touch  $\mathbf{M}$  at the points  $M_1, M_2, M_3$ .  $\theta_{M_1}, \theta_{M_2}$  correspond to stable equilibrium solutions whereas  $\theta_{M_3}$  is an unstable equilibrium solution.

### 2.3.1 Mechanical Regimes from Geometrical Viewpoint

Loading with a fixed horizontal confinement requires fixing  $X_o$  and varying  $Y_o$ . Following this protocol, we present the geometrical interpretation of the regimes *(i-iv)*.

**Regime (i)** – In Fig. 2.8(a), we show the result of following the procedure of fixing  $X_o$  and varying  $Y_o$  for  $X_o = 1.015$  ( $\epsilon_x = -0.015$ ). A set of circles  $\{\mathbf{C}\}$  (shown in the color blue) with their center lying on the vertical line  $x = X_o$  form a tangent to  $\mathbf{M}$ . The points of tangency are labeled by the black markers. As explained previously [Fig. 2.6(a)], these points correspond to (stable) equilibrium solutions,  $\theta_{eq}$ . For a number of such circular constructions we find  $\theta_{eq}$  and plot it against the vertical strain  $\epsilon_y$  in Fig. 2.8(b) (color black).  $\epsilon_y$  is calculated as  $1 - Y_o$ . As explained previously through Fig. 2.6(b), for lower values of  $Y_o$ , one finds two additional equilibrium states - one stable and one unstable. The corresponding tangential circles are not shown in Fig. 2.8(a) to avoid cluttering. We show these additional  $\theta_{eq}$  solutions in red in Fig. 2.8(b). The unstable states are shown in dashed. We now understand the genesis of the secondary solution branch for higher values of  $\epsilon_y$  [Fig. 2.4(a)]. We note that the primary branch (in black) corresponds to  $\theta < \tan^{-1}(a/b)$  and the secondary branch (in red) corresponds to  $\theta > \tan^{-1}(a/b)$ <sup>6</sup>.

Following the primary branch, the value of  $U$  initially decreases with  $\epsilon_y$ , reaches a minimum (at  $\theta = \tan^{-1}(b/a)$ ), and increases again.  $U(\epsilon_y)$  looks similar to Fig. 2.5(a).  $P(\epsilon_y)$  can be calculated as:  $P = \Delta U / \Delta \epsilon_y$ , which

<sup>6</sup>Note that at  $\theta = \tan^{-1}(a/b)$ , Eq. (2.11) is undefined.

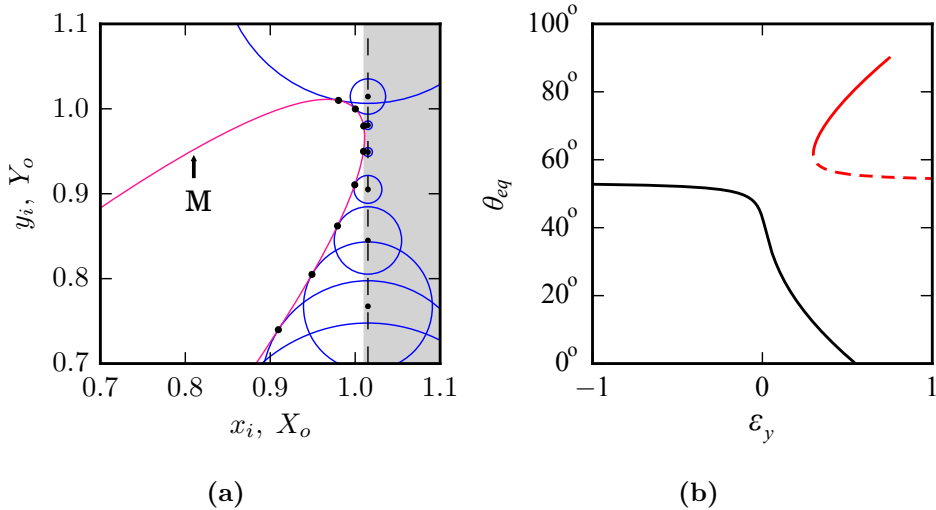


**Figure 2.8:** (a) The geometrical interpretation of regime (*i*). The set of tangential circles  $\{C\}$  (in blue) to  $M$  (in pink) centered on the line  $X_o = 1.015$  ( $\epsilon_x = -0.015$ ), touch  $M$  at the labeled black markers. The points of tangency denote the equilibrium states of the soft mechanism,  $\theta_{eq}$ . The shaded region belongs to the regime (*i*). (b)  $\theta_{eq}$  vs  $\epsilon_y$ . The primary branch is shown in black and the secondary branch is shown in red. Stable and unstable equilibria are shown in solid and dashed curve styles.

leads to a monotonic curve. The example corresponds to the regime (*i*). In fact the same arguments applies for any value of  $X_o$  within the gray-shaded region in Fig. 2.8(a).

**Regime (*ii*)** – Fig. 2.9(a) shows the geometrical approach for a smaller value of  $X_o = 0.99$  ( $\epsilon_x = 0.01$ ). In this case  $U$  reaches zero at two values of  $Y_o$ , which is where the line  $x = X_o$  intersects  $M$ . In between,  $U$  reaches a local maximum. Evidently, the graph of  $U$  vs  $\epsilon_y$  would appear similar to the one shown in Fig. 2.5(b). This example corresponds to the regime (*ii*). Just as in the previous case, one still finds the secondary equilibria branch for lower values of  $Y_o$ . Both the primary and the secondary state branches are shown in Fig. 2.9(b) on a  $\theta_{eq}(\epsilon_y)$  graph. In the previous section, we remarked that the ‘dip’ in the  $P(\epsilon_y)$  curve in Fig. 2.4(b) occurs because of the polarization switch from  $x$ -polarized state to  $y$ -polarized

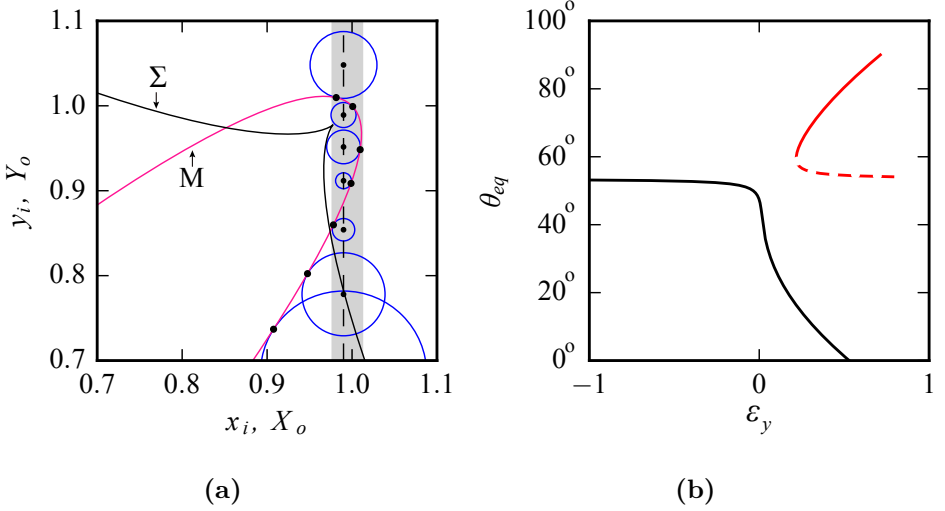


**Figure 2.9:** (a) The geometrical interpretation of regime **(ii)**. The set of tangential circles  $\{\mathbf{C}\}$  (in blue) to  $\mathbf{M}$  (in pink) centered on the line  $X_o = 0.99$  ( $\epsilon_x = 0.01$ ), touch  $\mathbf{M}$  at the labeled black markers. The points of tangency denote the equilibrium states of the soft mechanism,  $\theta_{eq}$ . The shaded region includes the values of  $X_o$  for regime **(ii)**. (b)  $\theta_{eq}$  vs  $\epsilon_y$ . The primary branch is shown in black and the secondary branch is shown in red. Stable and unstable equilibria are shown as solid and dashed curves respectively.

state.  $\theta_{eq}(\epsilon_y)$  graph substantiates the argument.  $\theta_{eq}(\epsilon_y = 0.0) > \pi/4$  making the mechanism initially  $x$ -polarized. The polarization state changes to  $y$ -polarized state ( $\theta_{eq}(\epsilon_y \gg 0.0) < \pi/4$ ) under the application of the load  $P$ .

The transition between the regime **(i)** and the regime **(ii)** occurs where the line  $x = X_o$  is tangent to the  $\mathbf{M}$ , at which point  $x = (x_i(\theta))_{max}$  i.e. the maximum value of  $x_i(\theta)$ . We know that  $\epsilon_x = 1 - X_o$ . An analytic expression for the critical value of horizontal strain  $(\epsilon_{xc})_{(i)-(ii)}$  marking the transition between regime **(i)** and regime **(ii)** can be given as:

$$(\epsilon_{xc})_{(i)-(ii)} = 1 - X_{o_{x=(x_i(\theta))_{max}}}. \quad (2.21)$$

We know that  $x_i(\theta) = a \cos(\theta) + b \sin(\theta)$ .  $x_i(\theta)$  attains a maximum value at

$\theta = \tan^{-1}(b/a)$ . Therefore,

$$(x_i(\theta))_{max} = a \cos \left( \tan^{-1} \left( \frac{b}{a} \right) \right) + b \sin \left( \tan^{-1} \left( \frac{b}{a} \right) \right). \quad (2.22)$$

Using the trigonometric identities:  $\cos(\tan^{-1} x) = \frac{1}{\sqrt{1+x^2}}$  and  $\sin(\tan^{-1} x) = \frac{x}{\sqrt{1+x^2}}$  and simplifying, we get:

$$(x_i(\theta))_{max} = \sqrt{a^2 + b^2}. \quad (2.23)$$

Therefore,

$$(\epsilon_{xc})_{(i)-(ii)} = 1 - \sqrt{a^2 + b^2}. \quad (2.24)$$

We will shortly show that the lower range of values of  $X_o$  which belong to regime **(ii)** are restricted unto where the vertical line  $x = X_o$  intersects the ‘nose’ of the evolute  $\Sigma$ . Hence, the shaded region in Fig. 2.9(a) corresponds to regime **(ii)**.

**Regime (iii)** – With a further decrease in the value of  $X_o$ , the vertical line  $x = X_o$  crosses the evolute  $\Sigma$  at three different points. Fig. 2.10(a) shows geometrical construction of tangential circles for one such case with  $X_o = 0.972$  ( $\epsilon_x = 0.028$ ). The present case is slightly non-trivial. We gradually decrease the value of  $Y_o$ , construct the *tangent circles*, and discuss the stability of the equilibrium states. For a proper demonstration, we make use of different colors. In Fig. 2.10(a), each  $(X_o, Y_o)$  and their point(s) of tangency are marked by a different color. We use the dashed curves to draw circles that correspond to unstable equilibrium. The first two equilibrium states are clearly stable (labeled by the *black* and *blue* markers). Consider now the case when the point  $(X_o, Y_o)$  lies on  $\Sigma$  (**D, C**, *red* marker). Emanating from this point, it is possible to construct two tangential circles. These circles touch **M** at the two labeled points  $D_M$  and  $C_M$ . The circles are shown in solid and dashed curve styles respectively because  $D_M$  corresponds to a stable equilibrium and  $C_M$  corresponds to an unstable equilibrium point. Similar is the argument for the other point  $(X_o, Y_o)$ , lying on  $\Sigma$  (**A, B**, *green* marker). Once again, two tangential circles touch **M** at  $A_M$  and  $B_M$  which correspond to unstable and stable states respectively. As a matter of course, every point on **M** which lies *between*  $A_M$  and  $C_M$  corresponds to an unstable equilibrium solution. The trajectory

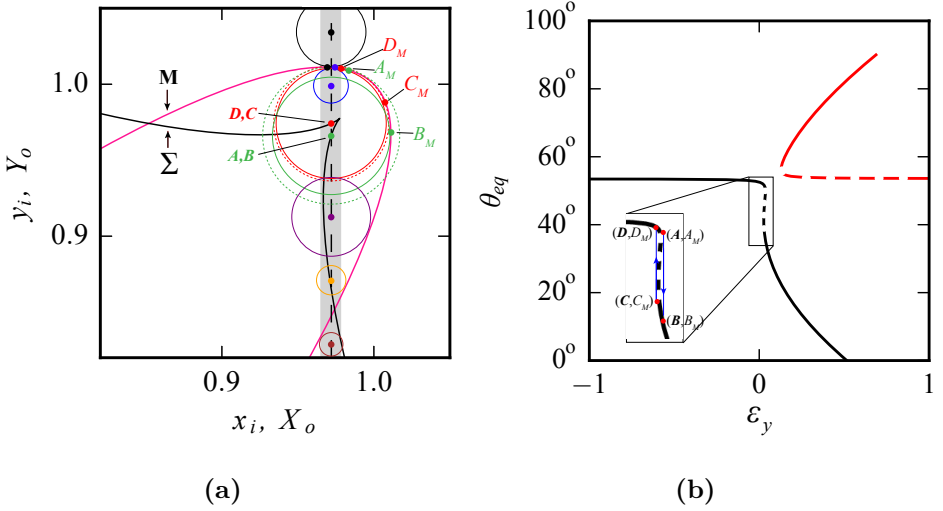


**Figure 2.10:** (a) (a) The geometrical interpretation of regime (*iii*). The set of tangential circles  $\{C\}$  (in blue) to  $M$  (in pink) centered on the line  $X_o = 0.972$  ( $\epsilon_x = 0.028$ ), touch  $M$  at the labeled black markers. The points of tangency denote the equilibrium states of the soft mechanism,  $\theta_{eq}$ . Shaded region belongs to the regime (*iii*). (b)  $\theta_{eq}$  vs  $\epsilon_y$ . The primary branch is shown in black and the secondary branch is shown in red. Stable and unstable equilibria are shown in solid and dashed curve styles. The primary branch encloses an unstable section, and multivaluedness is due to hysteresis.

of the mechanism along  $M$  from the point  $A_M$  to  $C_M$  corresponds to the movement from  $A$  to  $C$  of the point  $(X_o, Y_o)$  on the line  $x = X_o$ . This ‘reverse course’ is shown in dashed in Fig. 2.10(b). The result is an ‘enclosed’ unstable section on the primary branch. The points  $A, B, C, D$  are indeed the same points previously shown in Fig. 2.4(c), Fig. 2.5(c). We are in the regime (*iii*). In terms of  $\theta$ , the mechanism makes hysteretic jumps from  $A_M$  to  $B_M$  during loading and from  $C_M$  to  $D_M$  during unloading. For lower values of  $Y_o$ , the equilibrium are stable (shown in the color purple, orange and brown). And, similar to the regimes (*i*) and (*ii*), additional equilibria are born for an even lower values of  $Y_o$  (not shown in the figure).

The transition from regime (*ii*) to regime (*iii*) occurs where the line  $x = X_o$  just touches the cusp of  $\Sigma$ . This happens at  $\theta = \pi/4$ . The critical

value of the horizontal strain,  $(\epsilon_{xc})_{(ii)-(iii)}$  marking the transition between regime **(ii)** and regime **(iii)** is given by:

$$(\epsilon_{xc})_{(ii)-(iii)} = 1 - X_{o_{x_e=x_e(\theta=\pi/4)}}. \quad (2.25)$$

From Eq. (2.19), we can calculate  $x_e(\theta = \pi/4)$ . We know that  $x_i(\theta = \pi/4) = 1$ .

$$\begin{aligned} x_e(\theta = \pi/4) &= 1 - \frac{(a/\sqrt{2} - b/\sqrt{2})(a^2 + b^2 - 2ab)}{a^2 - b^2}, \\ &= 1 - \frac{(a - b)^2}{\sqrt{2}(a + b)}, \\ &= 1 - \frac{a^2 + b^2 - 2ab}{\sqrt{2}(a + b)}. \end{aligned} \quad (2.26)$$

Because we have set  $a + b = \sqrt{2}$ , squaring both sides, we get  $a^2 + b^2 = 2 - 2ab$ , we get:

$$x_e(\theta = \pi/4) = 2ab. \quad (2.27)$$

Therefore,

$$(\epsilon_{xc})_{(ii)-(iii)} = 1 - 2ab. \quad (2.28)$$

**Regime (iv)** – Fig. 2.11(a) shows the set of tangential circles  $\{C\}$  to  $\mathbf{M}$  whose center lies on the vertical line  $X_o = 0.96$  ( $\epsilon_x = 0.04$ ). Black markers show the corresponding equilibrium states. We only show the equilibrium solutions that lie on the primary solution branch. Additional equilibrium states also exist which form the secondary solution branch [Fig. 2.7(b)]. We plot the equilibrium solutions on the  $\theta_{eq}(\epsilon_y)$  graph [Fig. 2.11(b)].  $U$  exhibits a single global minima and attains a value of zero where the line  $x = X_o$  intersects  $\mathbf{M}$ . We are in the regime **(iv)**. Unlike the previous three cases, the primary equilibrium solutions admit  $\theta_{eq} > \tan^{-1}(a/b)$  while for the secondary solutions  $\theta_{eq} < \tan^{-1}(a/b)$ . In the vicinity of  $\tan^{-1}(a/b)$ , the solutions that were previously stable are now unstable and vice-versa. According to *bifurcation theory*, this corresponds to a *transcritical bifurcation* where at the critical value of the control parameter ( $\epsilon_x$ ), the two solutions meet and exchange stability. The transition between the regime **(iii)** and the regime **(iv)** occurs where the line  $x = X_o$  is tangent to the evolute  $\Sigma$ , at which point  $y = (y_i(\theta))_{max}$  i.e. the maximum value of  $y_i(\theta)$ . Therefore,

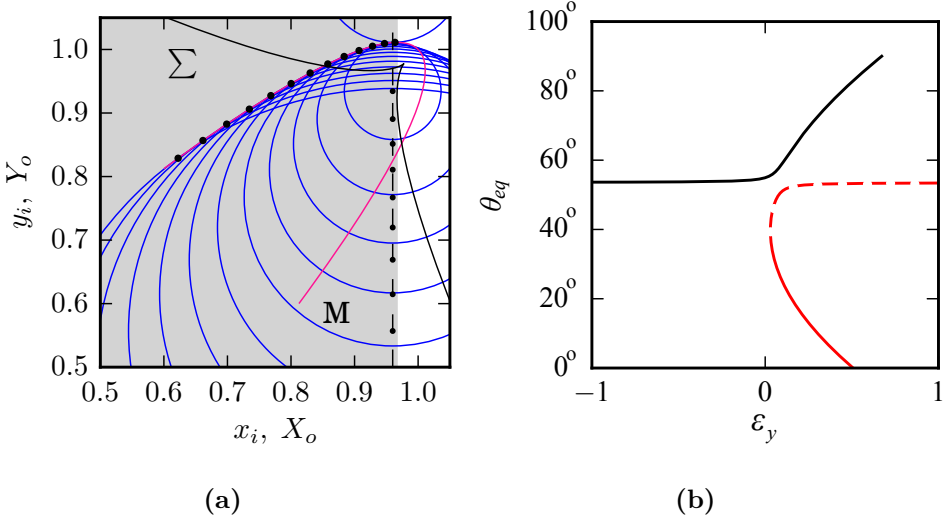


**Figure 2.11:** (a) The geometrical interpretation of regime *(iv)*. The set of tangential circles  $\{\mathbf{C}\}$  (in blue) to  $\mathbf{M}$  (in pink) centered on the line  $X_o = 0.96$  ( $\epsilon_x = 0.04$ ), touch  $\mathbf{M}$  at the labeled black markers. The points of tangency denote the equilibrium states of the soft mechanism,  $\theta_{eq}$ . Shaded region belongs to the regime *(iv)*. (b)  $\theta_{eq}$  vs  $\epsilon_y$ . The primary branch is shown in black and the secondary branch is shown in red. Stable and unstable equilibria are shown in solid and dashed curve styles.

the critical value of horizontal strain,  $(\epsilon_{xc})_{(iii)-(iv)}$ , marking the transition between regime *(iii)* and regime *(iv)* is given by:

$$(\epsilon_{xc})_{(iii)-(iv)} = 1 - X_{o_{x=(y_i(\theta))_{max}}}. \quad (2.29)$$

We know that  $y_i(\theta) = a \sin(\theta) + b \cos(\theta)$ .  $y_i(\theta)$  attains a maximum value at  $\theta = \tan^{-1}(a/b)$ . Therefore,

$$\begin{aligned} (y_i(\theta))_{max} &= a \sin\left(\tan^{-1}\left(\frac{a}{b}\right)\right) + b \cos\left(\tan^{-1}\left(\frac{a}{b}\right)\right), \\ &= \frac{2ab}{\sqrt{a^2 + b^2}}. \end{aligned} \quad (2.30)$$

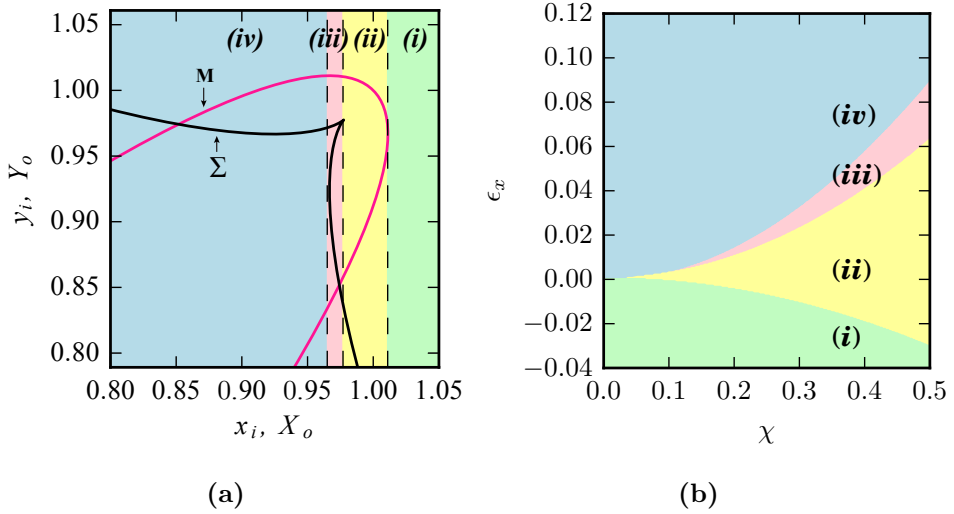


**Figure 2.12:** (a) For  $\chi = 0.30$ ,  $M$  and  $\Sigma$  shown in pink and black respectively. The regimes  $(i)$ - $(iv)$  are displayed in different colors and labeled. The dashed vertical lines demarcate the neighboring regimes. The critical value of  $\epsilon_{xc}$ , which marks the transition from regime  $(i)$  to  $(i+1)$  can be calculated as:  $(\epsilon_{xc})_{(i)-(i+1)} = 1 - X_{o(i)-(i+1)}$ . The generalized expressions for which are given by Eq. (2.24, 2.28, 2.31). (b) A regime transition plot for a range of  $\chi$  based on the generalized expressions for transition among the subsequent regimes  $(i)$ - $(iv)$ . The four regimes are labeled and shown in the different colors.

The analytical expression for the critical value of horizontal strain  $(\epsilon_{xc})_{(iii)-(iv)}$  is given as:

$$(\epsilon_{xc})_{(iii)-(iv)} = 1 - \frac{2ab}{\sqrt{a^2 + b^2}}. \quad (2.31)$$

For  $\chi = 0.30$ , we assemble the regimes  $(i)$ - $(iv)$  together in one plot and show them in Fig. 2.12(a).

**Regime transition plot** – The generalized analytical expressions derived in Eq. (2.24, 2.28, 2.31) provide clear-cut boundaries for  $\epsilon_{xc}$  which mark the transition between the successive regimes. We use these expressions to construct a *regime transition plot* for a range of values of  $\chi$ .

In Fig. 2.12(b), we plot  $\epsilon_{xc}$  for transitions between the regimes *(i)*-*(iv)* versus the biholarity  $\chi$ . We vary  $\chi$  from  $[0, 0.50]$ . We draw a couple of observations: *(i)* for low  $\chi$ , the distinction among the four regimes diminishes which results in their convergence at  $\epsilon_{xc} = 0.0$  for  $\chi \rightarrow 0$  - weak symmetry breaking leads to a weak nonlinear coupling between  $\epsilon_x$  and  $\epsilon_y$ , making the two non-monotonic regimes *(ii)*, *(iii)* vanish; monotonic regimes *(i)*, *(iv)* dominate. *(ii)* With an increase in  $\chi$ , we observe an expansion of the strain range over which regime *(ii)* prevails. This qualitatively matches with the experimental findings reported in [70], where it was found that for fixed ligament thickness  $t_l$ ,  $(\epsilon_{xc})_{(i)-(ii)}$  decreases with  $\chi$ .

### 2.3.2 A General Design Strategy

The above described geometrical interpretation of the soft mechanism provides with an inverse strategy to rationally design metamaterials with confinement controlled response. The scheme is stated below.

---

**Procedure** – An inverse strategy to rationally design mechanical metamaterials with confinement controlled response.

---

**Steps :**

- 1: First, formulate a continuous sequence of equilibria that emerges as the control parameter  $\epsilon_x$  is varied.
  - 2: Second, construct the involute (evolute) curve that is consistent with the sequence of these equilibria.
  - 3: Third, design a physical mechanism that posses this particular involute (evolute) trajectory, hypothetically which is possible as shown by Milton [24] - an extension of Kempe's universality theorem [72] for materials - where the main results states that "periodic structures made up of rigid bars and pivots can realize any given trajectory to an arbitrary high degree of approximation".
  - 4: Finally, based on the underlying mechanism, construct a soft deformable metamaterial with slender hinge connectors.
-

## 2.4 Modeling the Finite Thickness Interhole Ligaments with Torsional Springs

Previously, we did not take into account the thickness of the interhole ligaments,  $t_l$  [Fig. 2.1(a)] and assumed the hinges in the mechanism to be ideal with zero energy costs for bending. In this section, we model the finite thickness of the interhole ligaments by coupling the hinges of the soft mechanism with torsional springs of  $\pi/2$  rest angle. In this way, we introduce an additional penalty to change  $\theta$  away from the neutral state,  $\theta = \pi/4$ . The total internal energy  $U$  now contains an extra term accounting for the bending energy stored in the torsional springs,  $E_t$ .

$$U = E_x + E_y + E_t, \quad (2.32)$$

where  $E_x$  and  $E_y$  are the elastic energies stored in the horizontal and vertical springs and are the same as given by Eq. (2.9) and Eq. (2.13) respectively. We will use the notation  $E_l$  to denote the total elastic energy stored in the linear springs,  $E_l = E_x + E_y$ .  $E_t$  at a general angle  $\theta$  is given by:

$$\begin{aligned} E_t &= 2 \times \left(\frac{1}{2}\right) \times k_t \left(2\theta - \frac{\pi}{2}\right)^2 + 2 \times \left(\frac{1}{2}\right) \times k_t \left(\frac{\pi}{2} - 2\theta\right)^2, \\ &= 8k_t \left(\theta - \frac{\pi}{4}\right)^2. \end{aligned} \quad (2.33)$$

$E_t$  is quadratic in  $\theta$  with the minimum located at  $\theta = \pi/4$ . The expression for  $U$  is given as:

$$U = 2k_x (\epsilon_x + x_i(\theta) - 1)^2 + \frac{P^2}{2k_y} + 8k_t \left(\theta - \frac{\pi}{4}\right)^2, \quad (2.34)$$

where  $k_x$ ,  $k_y$  and  $k_t$  are the horizontal, vertical and torsional spring constants respectively,  $\epsilon_x$  is the external  $x$ -confinement,  $P$  is the load, and the expressions for  $x_i(\theta)$  and  $y_i(\theta)$  are given by Eq. (2.7), Eq. (2.8) respectively. We aim to derive an expression for  $P$ , the approach for which is same as described in §2.2.1, following which, we obtain:

$$P = \frac{-2k_x (\epsilon_x + x_i(\theta) - 1) (-a \sin \theta + b \cos \theta) - 4k_t (2\theta - \pi/2)}{(a \cos \theta - b \sin \theta)}. \quad (2.35)$$

The expression for  $\epsilon_y$  is the same as earlier and is given by the Eq. (2.12).

With the help of an example, we now demonstrate the effect of  $k_t$  on the energy curves -  $E_l, E_t$  and  $U$ . In Fig. 2.13, energy curves are shown as a function of  $\epsilon_y$ , and as a function of  $\theta$  in Fig. 2.14 for a system with  $\chi = 0.30$ . Within each figure,  $E_l, E_t$  and  $U$  are shown in the color red, green and blue respectively. Note that only the primary equilibrium solution branches are shown. Fig. 2.13(a) displays the energy curves for  $\epsilon_x = 0.028$  and  $k_t = 0.0$ . In this case,  $U = E_l$  and the system is in regime (*iii*).  $U$  exhibits two global minima where  $U = 0$ . These minima exist on both the sides of  $\theta = \pi/4$  in  $U(\theta)$  plot [Fig. 2.14(a)]. Recall from the geometrical interpretation that this happens precisely where the vertical line  $x = 0.028$  intersects the trajectory curve  $\mathbf{M}$  [Fig 2.10(a)]. We now increase  $k_t$ , keeping  $\epsilon_x$  fixed at 0.028. Fig. 2.13(b) shows the energy curves for  $k_t = 5 \times 10^{-4}$ . An emerging trend in the  $U(\theta)$  curves should be noticed: an increase in the value of  $k_t$  gradually ‘elevates’ the energy landscape. In Fig. 2.14(b), we notice the gradual elimination of the minimum in  $U$  for  $\theta < \pi/4$ . The system is still in regime (*iii*), however. This, we confirm by plotting the force curves,  $P(\epsilon_y)$ . Utilizing the Eq. (2.34), Fig. 2.15 shows  $P(\epsilon_y)$  for the same system as in Fig. 2.13 and Fig. 2.14.  $P(\epsilon_y)$  in Fig. 2.15(a-b) is typical of regime (*iii*) - a non-monotonic multi-valued curve.

With a further increase in the value of  $k_t$ , its effect on the energy landscape grows. Fig. 2.13(c) and Fig. 2.14(c) shows the energy curves for  $k_t = 3 \times 10^{-3}$ . At this value of  $k_t$ , the nature of  $P(\epsilon_y)$  is non-monotonic but single-valued [Fig. 2.15(c)] - characteristic of regime (*ii*). Ultimately for a high enough value of  $k_t = 8 \times 10^{-3}$  [Fig. 2.13(d) and Fig. 2.14(d)],  $U(\epsilon_y)$  ceases to display any sharp curvature change. The derivative of it,  $P(\epsilon_y)$  is monotonic [Fig. 2.15(d)]. The system now is in regime (*i*). We conclude that high values of  $k_t$  push the mechanical response towards the regime (*i*).

**Regime transition plots with torsional springs** – Torsional springs alter the values of  $\epsilon_{xc}$ , the critical horizontal strain values marking the transition among the successive regimes. We have already demonstrated that an increase in the value of  $k_t$  pushes the mechanical response of the system towards the regime (*i*); the values of  $\epsilon_{xc}$  are expected to shift-up with  $k_t$ . Fig. 2.16 shows the regime transition plots for  $k_t = 3 \times 10^{-3}$  in (a) and for  $k_t = 8 \times 10^{-3}$  in (b). The values of  $\epsilon_{xc}$  are now captured numerically unlike in Fig. 2.12(b), where we utilized direct analytical expressions. We

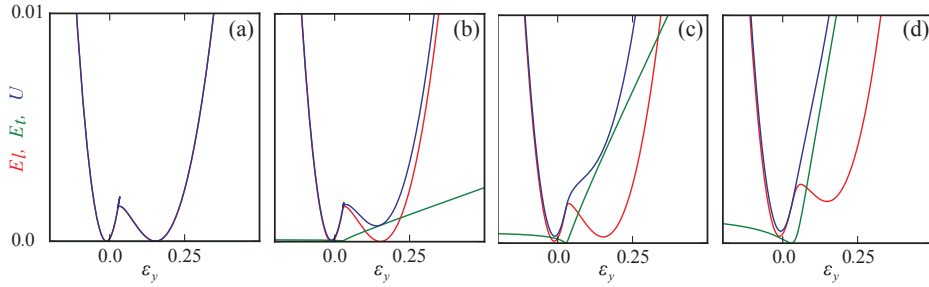


**Figure 2.13:** Energy curves shown as a function of  $\epsilon_y$  for a system with  $\chi = 0.30$ ,  $\epsilon_x = 0.028$  and increasing values of  $k_t$ .  $E_l, E_t$  and  $U$  denote the elastic energy stored in the linear springs, torsional springs and total internal energy of the system and are shown in the color red, green and blue respectively. Note that we only show the primary solution branches. (a)  $k_t = 0.0$ ,  $U = E_l$ . The plot is familiar [Fig. 2.5(c)]. The system is in the regime **(iii)**. (b)  $k_t = 5 \times 10^{-4}$ ,  $U(\epsilon_y)$  displays multivaluedness and hysteresis. The system is in regime **(iii)** still. (c)  $k_t = 3 \times 10^{-3}$ ,  $U(\epsilon_y)$  displays curvature change. The system is in regime **(ii)**. (d)  $k_t = 8 \times 10^{-3}$ ,  $U(\epsilon_y)$  consists of a single global minimum with no curvature change. The system now is in regime **(i)**.

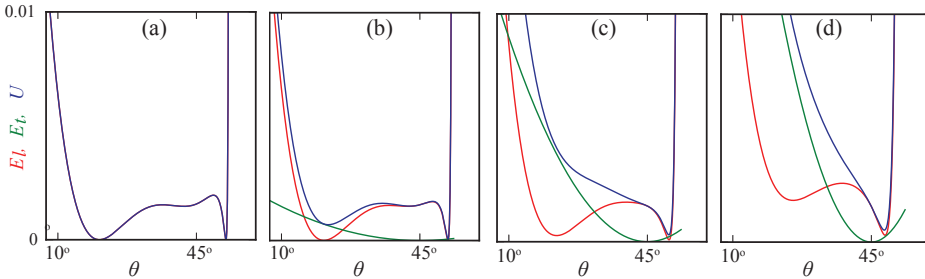


**Figure 2.14:** Energy curves shown as a function of  $\theta$  for a system with  $\chi = 0.30$ ,  $\epsilon_x = 0.028$  and for the same four values of  $k_t$  as in Fig. 2.13. Symbols have the same meaning. We notice an emerging trend from (a)-(d) as the value of  $E_t$  dominates over  $E_l$ : gradual elevation of the minimum in  $U$  that exist on the either side of  $\theta = 45^\circ$ . As  $E_t$  has a minimum at  $\theta = 45^\circ$ , the minimum for  $\theta < 45^\circ$  gets strongly affected.

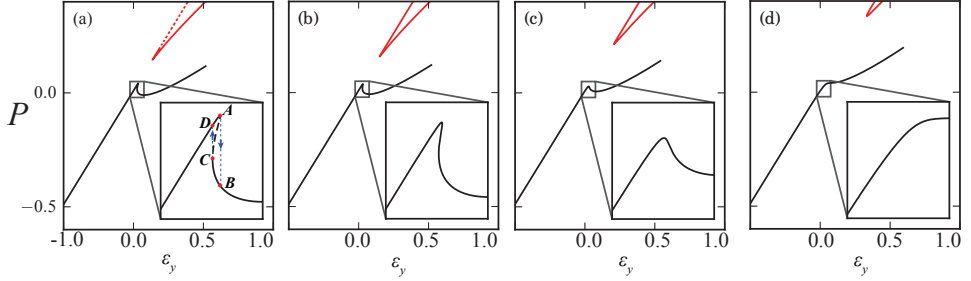


**Figure 2.15:**  $P(\epsilon_y)$  for a system with  $\chi = 0.30$ ,  $\epsilon_x = 0.028$  and for increasing values of  $k_t$ . (a)  $k_t = 0.0$ , and (b)  $k_t = 5 \times 10^{-4}$ .  $P(\epsilon_y)$  displays multi-valued owing to the hysteretic behavior in both the figures. The system is in the regime **(iii)**. (c)  $k_t = 3 \times 10^{-3}$ ,  $P(\epsilon_y)$  is non-monotonic. The system is in the regime **(ii)**. (d)  $k_t = 8 \times 10^{-3}$ ,  $P(\epsilon_y)$  is monotonic. The system is in the regime **(i)**. We conclude that with an increase in the values of  $k_t$ , the mechanical response shifts towards regime **(i)**.

fix the value of  $\chi$ , the  $\epsilon_{xc}$  values for transition between the consecutive regimes are then captured based on the change in the trajectory of the  $P(\epsilon_y)$  curves. We notice the expected upward shift in the regime domains. It is worth noting that (i) an increase in the values of critical strain value,  $(\epsilon_{xc})_{(i)-(ii)}$  which marks onset of regime **(ii)** with ligament thickness  $t_l$  and fixed  $\chi$  is also observed in [70], (ii) increase in  $k_t$  makes the existence of all the four regimes for non-negative  $\epsilon_x$  values, making them consistent with the experiments [Fig. 2.2].

We further characterize the results by plotting a variation in  $\epsilon_{xc}$  with  $k_t$  for three different values of  $\chi$  in Fig. 2.17 - (a)  $\chi = 10^{-3}$ , (b)  $\chi = 0.30$ , (c)  $\chi = 0.50$ . There, within each figure, we show  $(\epsilon_{xc})_{(i)-(ii)}$  in blue,  $(\epsilon_{xc})_{(ii)-(iii)}$  in green and  $(\epsilon_{xc})_{(iii)-(iv)}$  in red. We draw several conclusions. (i) For  $\chi = 10^{-3}$  [Fig. 2.17(a)], we do not observe the prevalence of non-monotonic regimes but effectively only the regimes **(i)** and **(iv)** exist. The scaling of  $\epsilon_{xc}$  with  $k_t$  is linear with slope  $\approx 4.0$ . We attempt to justify this in the next section. (ii) For  $\chi = 0.30, 0.50$  [Fig. 2.17(b,c)], we observe that  $\epsilon_{xc}$  for all the regime transitions scales linearly, although their slope values vary in a slightly complicated manner. Fig. 2.17(d) shows the variation in these slope values versus the biholarity  $\chi$ . We vary  $\chi$  in the range  $[0, 1]$ . Immediately we can notice that for  $\chi \rightarrow 0$ , the distinction among the four regimes

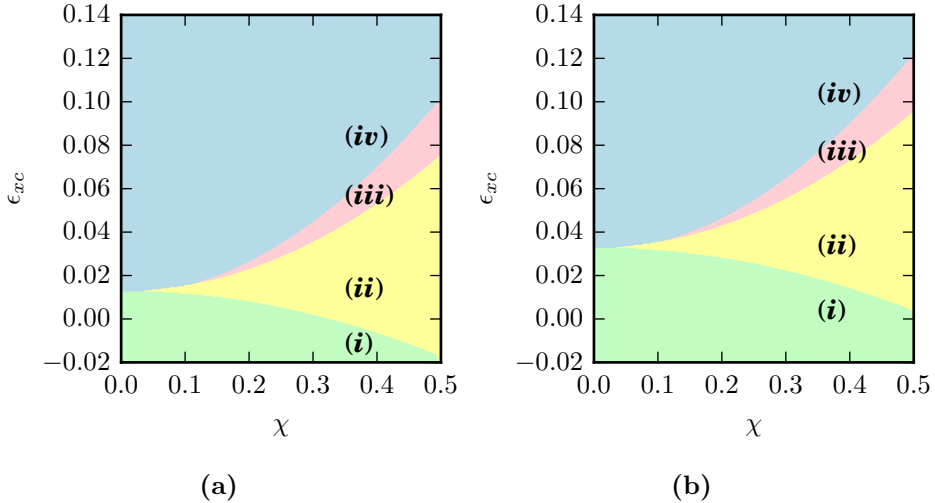


**Figure 2.16:** The effect of torsional spring constant  $k_t$  on  $\epsilon_{xc}$ , the critical horizontal strain values that separate the contiguous regimes (*i-iv*). (a)  $k_t = 3 \times 10^{-3}$ , (b)  $k_t = 8 \times 10^{-3}$ . Regimes (*i-iv*) are labeled and shaded in different colors. Overall, we observe that for all biolarity  $\chi$ , an increase in  $k_t$  shifts  $\epsilon_{xc}$  towards higher values. We duly characterize our findings in Fig. 2.17.

vanishes and the value of  $\Delta\epsilon_{xc}/\Delta k_t \rightarrow 4$ . Moving away towards higher  $\chi$  values, we interestingly notice that  $(\Delta\epsilon_{xc}/\Delta k_t)_{(ii)-(iii)}$  is not dependent on  $\chi$  and maintains a constant value equal to 4.  $(\Delta\epsilon_{xc}/\Delta k_t)_{(i)-(ii)}$  and  $(\Delta\epsilon_{xc}/\Delta k_t)_{(iii)-(iv)}$ , however exhibit an exponential increase with  $\chi$ , with the effect being stronger in the former than later.

## 2.5 Weak Symmetry Breaking in Monoholar Systems

In this section, we probe the limiting case where the biolarity  $\chi$ , of the system approaches the value zero. We remember that  $\chi$  serves as a measure of the relative difference between the diameters of the two neighboring holes (§2.2). We first briefly introduce the case where the holes are of exactly the same size, and through the help of concepts from *bifurcation theory*,

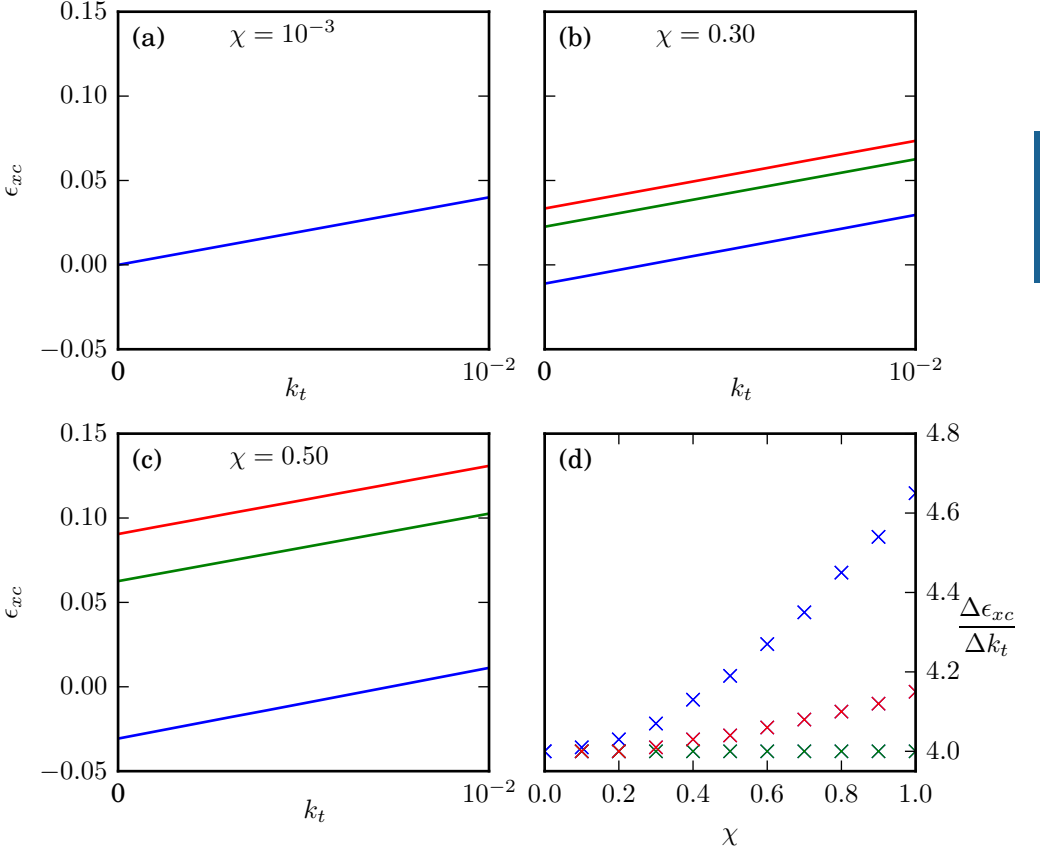


**Figure 2.17:** (a-c) The scaling of  $\epsilon_{xc}$  with  $k_t$  for different  $\chi$  values. (a)  $\chi = 10^{-3}$ , (b)  $\chi = 0.30$  and (c)  $\chi = 0.50$ . Within each figure,  $(\epsilon_{xc})_{(i)-(ii)}$  is shown in blue,  $(\epsilon_{xc})_{(ii)-(iii)}$  is shown in green and  $(\epsilon_{xc})_{(iii)-(iv)}$  is shown in red. The variation of slopes of these linear curves is shown in (d). We observe that  $(\Delta\epsilon_{xc}/\Delta k_t)_{(ii)-(iii)}$  is independent of  $\chi$  and maintains a constant value equal to 4.  $(\Delta\epsilon_{xc}/\Delta k_t)_{(i)-(ii)}$  and  $(\Delta\epsilon_{xc}/\Delta k_t)_{(iii)-(iv)}$ , however exhibit an exponential increase with  $\chi$ . The distinction among the four regimes vanishes for  $\chi \rightarrow 0$  with  $\Delta\epsilon_{xc}/\Delta k_t \rightarrow 4$ .

show how the original pitchfork bifurcation structure gets disturbed upon inducing small symmetry breaking by making the hole sizes slightly unequal. This is called *unfolding* of the bifurcation. We derive the equation describing

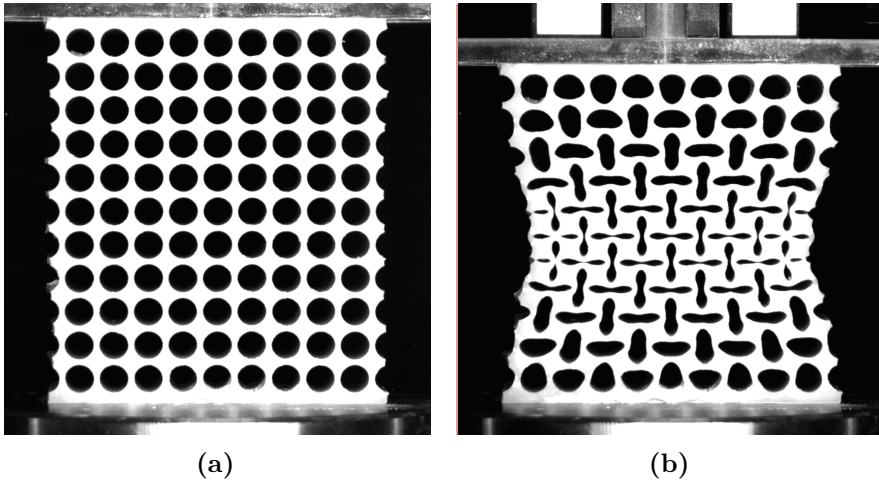


**Figure 2.18:** (a) Monoholar sheet: an elastic slab perforated with an alternating pattern of equi-sized circular holes on a square array. (b) When compressed beyond a critical value of the vertical strain, the monoholar sheet undergoes a pattern transformation triggered by elastic instability and reaches a state of mutually orthogonal ellipses. Monoholar sheet exhibits a negative value of the Poisson’s ratio ( $\mu$ ) [74] and forms a classical example of the auxetic materials. The hole diameter of the sample is 8.5 mm, the connector filament thickness (previously denoted by  $t_l$  for the biholar sheet) is 1.5 mm and the out-of-plane thickness of the sample is 35 mm. These images are adopted from [73].

this unfolding in §2.5.1 and deploy it to understand the case where  $\chi \rightarrow 0$  in §2.5.2. We ultimately provide with a justification for the observed value of  $(\Delta\epsilon_{xc}/\Delta k_t) \rightarrow 4.0$  for  $\chi \rightarrow 0$  in the previous section [Fig. 2.17(d)].

**Monoholar sheet,  $\chi = 0$**  – Fig. 2.18(a) shows a quasi-2D elastic slab patterned with equal sized circular holes [73]. We call this a *monoholar sheet*. The hole diameter of the sample is 8.5 mm, the connector filament thickness (previously denoted by  $t_l$  for the biholar sheet) is 1.5 mm and the out-of-plane thickness of the sample is 35 mm. A monoholar sheet with finite interhole ligament thickness such as this undergoes an initial gradual and homogeneous compression in the linear elastic range, where the circular holes deform in a uniform fashion. Upon reaching a critical vertical strain,

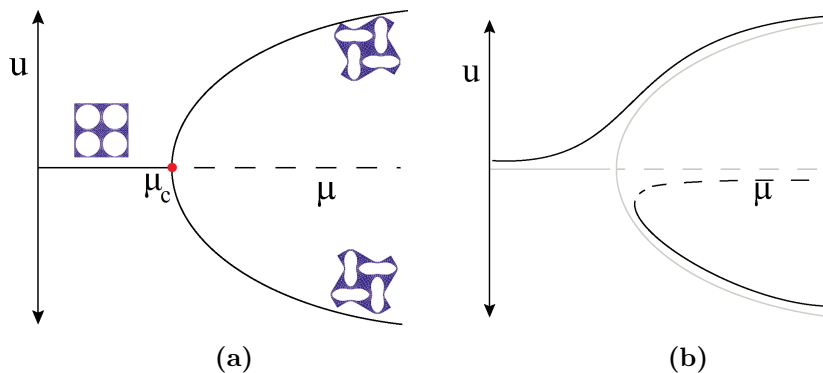


**Figure 2.19:** (a) Compression of a monoholar sheet illustrated through a perfect pitchfork bifurcation diagram. The vertical axis ( $u$ ) represents the angular displacement of the ‘center line’ connecting the interhole ligaments and the horizontal axis ( $\mu$ ) denotes the vertical compression. Beyond the critical value  $\mu_c$ , there is equal probability that the system forms either of the two (shown) elliptic arrangements. (b) Introduction of slight symmetry breaking into the system,  $\chi \neq 0$  disturbs the original bifurcation diagram, making it imperfect. The system displays a tendency to follow either of the two non-trivial solutions. In the two diagrams, the stable and the unstable equilibria are shown in solid and dashed curves respectively.

the interhole ligaments undergo a buckling instability, thereby triggering a pattern transformation to a state with mutually orthogonal ellipses [Fig. 2.18(b)] [74]. After buckling, the stability gets transferred from the original symmetric state to the symmetry broken state. If the memory effects are discounted, the alternating polarization pattern of the elliptical holes is completely arbitrary because of the equal likeliness of a particular ellipse to orient its major axis along the  $x$ -direction or along the  $y$ -direction. In bifurcation theory, this case of equal likeliness of a system to follow either of the two solution branches once the critical value of a control parameter (vertical strain in this case) is reached is referred to as the system being at the *bifurcation point* of a *perfect pitchfork bifurcation* [75].

The situation can be illustrated through a pitchfork bifurcation diagram [Fig 2.19(a)]<sup>7</sup>. The vertical axis,  $u$  represents the state of the system such as the angular displacement of the ‘center line’ connecting the neighboring

<sup>7</sup>We explain this case mathematically in §2.5.2.

elastic units, while the horizontal axis,  $\mu$  denotes the vertical compression. In the diagram, the stable equilibrium solution branches are shown in solid while the unstable branches are shown in dashed. One usually concentrates on the stable solutions since these are the only ones one observes in experiments [76]. For  $\mu < \mu_c$ , the critical value of the *control parameter*, there is only one equilibrium solution branch - corresponding to elastic compression without any formation of the elliptic pattern. Beyond  $\mu_c$ , this solution becomes unstable and instead two new stable solutions are born. These new solutions correspond to the two ‘oppositely’ buckled states, wherein the holes are oppositely polarized and which are equally likely to occur.

**Perturbed monoholar sheet,  $\chi \neq 0$ .** Imperfect bifurcation diagrams occur when small symmetry breaking terms destroy the original bifurcation structure [77]. Weak symmetry breaking leads to an *imperfect* pitchfork bifurcation, causing the system to prefer one of the two solution branches [Fig 2.19(b)]. A monoholar system with a weak symmetry breaking,  $\chi \neq 0$  forms one such example. Upon compression, the mutually orthogonal ellipse pattern is no longer arbitrarily selected by the bifurcation but in fact can be manipulated. Specifically from the point of view of confinement controlled experiments, the polarization pattern depends on the values of strains in the horizontal and vertical directions. Unlike for a perfect monoholar system, where the horizontal strain  $\epsilon_x$  and the vertical strain  $\epsilon_y$  play a similar role, in a system with broken symmetry, these strains each favor a different polarization of the pattern (§2.1, [Fig. 2.1(b,c)]). Their interactions typically results in the system to prefer one out of the two stable solution branches. The interactions between these two branches result in the complex mechanics of a confined biholar sheet [20].

Several bifurcation scenarios emerge as we perturb the perfect monoholar system and vary the parameters  $\epsilon_x$  and  $\epsilon_y$ . These scenarios arise from the unfolding of the pitchfork bifurcation [75]. To understand the local bifurcation scenarios, in the following section, we probe the system for the limiting case. Our aim is to obtain a *general equation* valid around the singular point that provides us with the complete description of the nature of the bifurcations and transitions. We will establish that the general equation resembles the *normal form*<sup>8</sup> of an imperfect pitchfork bifurcation

<sup>8</sup>Normal form of a bifurcation are in a sense, the simplest possible polynomial equation which contains the bifurcation [77].

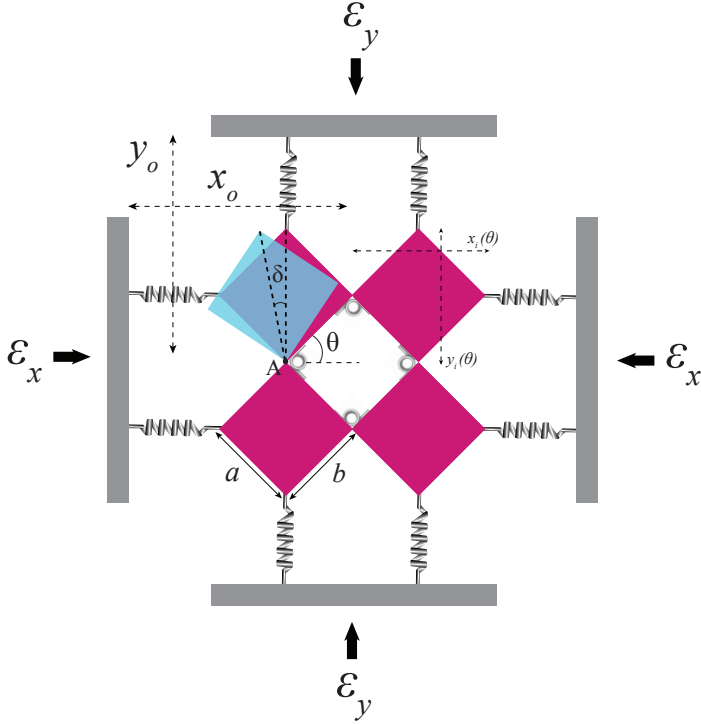


**Figure 2.20:** Soft mechanism for a monoholar system,  $\chi \rightarrow 0$  ( $a \approx b$ ) consisting of pin-jointed squares. We examine the system for small torsional spring constant  $k_t$  and small angular displacement  $\delta$ .

and utilize this equation to describe the physics of the perfect monoholar as well as a perturbed monoholar system. To this end, we exploit the soft mechanism for a system with  $\chi \rightarrow 0$  under external loading [Fig. 2.20] and conduct the analysis for weak angular displacements by following an approach based on the method of *Lagrange multipliers*.

### 2.5.1 Soft Mechanism for a Perturbed Monoholar System

In this section, we derive an equation describing the equilibrium states of the mechanism shown in Fig. 2.20 under the application of horizontal strain  $\epsilon_x$  and vertical strain  $\epsilon_y$  for small torsional spring constant  $k_t$  and small biholarity  $\chi$ . To achieve this, we minimize the total internal energy

of the system,  $U$  [Eq. (2.32)], subjected to geometrical constraints in the horizontal and vertical directions. The Lagrangian  $\mathcal{L}$  can be expressed as:

$$\begin{aligned}\mathcal{L} &= U + \lambda_1 C_1 + \lambda_2 C_2, \\ &= E_x + E_y + E_t + \lambda_1 C_1 + \lambda_2 C_2,\end{aligned}\tag{2.36}$$

where the familiar symbols:  $E_x$ ,  $E_y$  and  $E_t$  have the same meaning as previous (§2.4).  $\lambda_1$  and  $\lambda_2$  are the Lagrange multipliers for the associated geometrical constraints  $C_1$  and  $C_2$ . Below, we explain these constraints.

**Horizontal constraint  $C_1$**  – Let  $l_{i,h}$  denote the rest length of the horizontal springs. For the initial state of the mechanism, we can then write:

$$l_{i,h} + x_i(\pi/4) = x_o\tag{2.37}$$

where  $x_i(\pi/4)$  is the initial  $x$ -dimension of the rigid unit of the mechanism [Eq. (2.7)]. Suppose that upon the application of a small horizontal strain,  $\epsilon_x$ , the diagonal of the rigid unit rotates about the point  $A$  by a small angle  $\delta$ . One can then write:

$$\epsilon_x + l_{f,h} + x_i(\pi/4 + \delta) = x_o,\tag{2.38}$$

where  $l_{f,h}$  denotes the final length of the horizontal spring upon the application of  $\epsilon_x$ . We denote the net change in the length of the springs by  $e_x$ , given by:

$$\begin{aligned}e_x &= l_{i,h} - l_{f,h}, \\ &= \epsilon_x + x_i(\pi/4 + \delta) - 1.\end{aligned}\tag{2.39}$$

Using Eq. (2.7), we can expand  $x_i(\pi/4 + \delta)$  and write  $e_x$  as:

$$\begin{aligned}e_x &= \epsilon_x + a \cos(\pi/4 + \delta) + b \sin(\pi/4 + \delta) - 1, \\ &= \epsilon_x + \cos \delta - \frac{\sin \delta(a - b)}{\sqrt{2}} - 1.\end{aligned}\tag{2.40}$$

We term  $(a - b)/\sqrt{2}$  as *symmetry breaking parameter* and denote it with  $m$ . For a monoholar system,  $m$  takes on the value zero. Substituting  $(a - b)/\sqrt{2}$  with  $m$ , the above equation can be written as:

$$e_x = \epsilon_x + \cos \delta - m \sin \delta - 1\tag{2.41}$$

The constraint  $C_1$  is therefore given by:

$$C_1 = e_x - \epsilon_x - \cos \delta + m \sin \delta + 1 = 0. \quad (2.42)$$

**Vertical constraint  $C_2$**  – Similarly, we impose the geometrical constraint for the vertical direction and find that:

$$C_2 = e_y - \epsilon_y - \cos \delta - m \sin \delta + 1 = 0. \quad (2.43)$$

**Expressions for  $E_x$ ,  $E_y$  and  $E_t$**  – The energy stored in the horizontal springs,  $E_x$  can be expressed as:

$$E_x = 4 \times \frac{1}{2} k_x e_x^2 = 2k_x (\epsilon_x + \cos \delta - m \sin \delta - 1)^2. \quad (2.44)$$

The energy stored in the vertical springs,  $E_y$  is given by:

$$E_y = 4 \times \frac{1}{2} k_y e_y^2 = 2k_y (\epsilon_y + \cos \delta + m \sin \delta - 1)^2. \quad (2.45)$$

The energy stored in the torsional springs,  $E_t$  is given by:

$$E_t = 4 \times \frac{1}{2} k_t \times (2\delta)^2 = 8k_t \delta^2. \quad (2.46)$$

Using Eq. (2.42)-(2.46), the Lagrangian,  $\mathcal{L}$  [Eq. (2.36)] can now be written as:

$$\begin{aligned} \mathcal{L} = & 2k_x (\epsilon_x + \cos \delta - m \sin \delta - 1)^2 + 2k_y (\epsilon_y + \cos \delta + m \sin \delta - 1)^2 + 8k_t \delta^2 \\ & + \lambda_1 (e_x - \epsilon_x - \cos \delta + m \sin \delta + 1) + \lambda_2 (e_y - \epsilon_y - \cos \delta - m \sin \delta + 1). \end{aligned} \quad (2.47)$$

We impose the following equilibrium conditions in order to maintain quasi-staticity:

$$\frac{\partial \mathcal{L}}{\partial e_x} = 0 \implies \lambda_1 = -4k_x(\epsilon_x + \cos\delta - m\sin\delta - 1) \quad (2.48)$$

$$, \frac{\partial \mathcal{L}}{\partial e_y} = 0 \implies \lambda_2 = -4k_y(\epsilon_y + \cos\delta + m\sin\delta - 1) \quad (2.49)$$

$$\begin{aligned} \frac{\partial \mathcal{L}}{\partial(\delta)} = 0 \implies & 4k_x(\epsilon_x + \cos\delta - m\sin\delta - 1)(-\sin\delta - m\cos\delta) + \\ & 4k_y(\epsilon_y + \cos\delta + m\sin\delta - 1)(-\sin\delta + m\cos\delta) + \\ & 16k_t\delta + \lambda_1(\sin\delta + m\cos\delta) + \\ & \lambda_2(\sin\delta - m\cos\delta) = 0. \end{aligned} \quad (2.50)$$

Substituting the values of  $\lambda_1$  and  $\lambda_2$  from Eq. (2.48) and Eq. (2.49) respectively in the Eq. (2.50), we obtain:

$$\begin{aligned} & k_x(\epsilon_x + \cos\delta - m\sin\delta - 1)(\sin\delta + m\cos\delta) + \\ & k_y(\epsilon_y + \cos\delta + m\sin\delta - 1)(\sin\delta - m\cos\delta) - 2k_t\delta = 0. \end{aligned} \quad (2.51)$$

We set  $k_x = k_y = k_l$  and obtain:

$$\begin{aligned} & (\epsilon_x + \cos\delta - m\sin\delta - 1)(\sin\delta + m\cos\delta) + \\ & (\epsilon_y + \cos\delta + m\sin\delta - 1)(\sin\delta - m\cos\delta) - \frac{2k_t\delta}{k_l} = 0. \end{aligned} \quad (2.52)$$

Since we are interested in small angular displacements, we expand the expressions for  $\sin\delta$  and  $\cos\delta$  around  $\delta = 0$  up to the third order, and thus writing  $\sin\delta$  as  $\delta - \delta^3/6$  and  $\cos\delta$  as  $1 - \delta^2/2$ , we obtain:

$$\begin{aligned} & \left( \epsilon_x - \frac{\delta^2}{2} - m\delta + m\frac{\delta^3}{6} \right) \left( \delta - \frac{\delta^3}{6} + m - m\frac{\delta^2}{2} \right) + \\ & \left( \epsilon_y - \frac{\delta^2}{2} + m\delta - m\frac{\delta^3}{6} \right) \left( \delta - \frac{\delta^3}{6} - m + m\frac{\delta^2}{2} \right) - \frac{2k_t}{k_l}\delta = 0. \end{aligned} \quad (2.53)$$

Simplifying the above equations and neglecting the terms higher than  $\delta^3$  and  $m$ , we end up with the final equation:

$$m(\epsilon_x - \epsilon_y) + (\epsilon_x + \epsilon_y - \frac{2k_t}{k_l})\delta - \frac{m}{2}(\epsilon_x - \epsilon_y)\delta^2 - \left(\frac{\epsilon_x}{6} + \frac{\epsilon_y}{6} + 1\right)\delta^3 = 0. \quad (2.54)$$

Reorganizing the above equation, we obtain:

$$\frac{m(\epsilon_x - \epsilon_y)}{\left(\frac{\epsilon_x}{6} + \frac{\epsilon_y}{6} + 1\right)} + \frac{(\epsilon_x + \epsilon_y - \frac{2k_t}{k_l})}{\left(\frac{\epsilon_x}{6} + \frac{\epsilon_y}{6} + 1\right)}\delta - \frac{m}{2} \frac{(\epsilon_x - \epsilon_y)}{\left(\frac{\epsilon_x}{6} + \frac{\epsilon_y}{6} + 1\right)}\delta^2 - \delta^3 = 0. \quad (2.55)$$

We recognize this as an unfolding of a pitchfork bifurcation. The normal form of a perfect (*supercritical*) pitchfork bifurcation is given by:

$$\mu u - u^3 = 0, \quad (2.56)$$

where  $u$  characterizes the state of the system and  $\mu$  is the bifurcation parameter. The normal form of a perturbed pitchfork bifurcation is given by:

$$\alpha + \mu u - \beta u^2 - u^3 = 0, \quad (2.57)$$

where,  $\alpha$  and  $\beta$  are two real unfolding parameters [78]. Clearly, Eq. (2.55) resembles the normal form of an imperfect pitchfork bifurcation. We further confirm this by plotting a bifurcation diagram in the  $(\epsilon_y, \delta)$  space. We can reshuffle Eq. (2.55) and express  $\epsilon_y$  explicitly as a function of  $\delta$  and other parameters:

$$\epsilon_y = \frac{m\epsilon_x + \left(\epsilon_x - \frac{2k_t}{k_l}\right)\delta - m\epsilon_x \frac{\delta^2}{2} + \left(\frac{-\epsilon_x}{6} - 1\right)\delta^3}{\left(m - \delta - m\frac{\delta^2}{2} + \frac{\delta^3}{6}\right)}. \quad (2.58)$$

We use the above equation to plot the bifurcation diagram shown in Fig. 2.21 for a system with  $m = 10^{-2}$ ,  $k_t = 0$  and for a range of small values of horizontal strain  $\epsilon_x$  (see colorbar on the right) and confirm visually that indeed Eq. (2.55) represents unfolding of a pitchfork bifurcation as we vary  $\epsilon_x$ . In principle, the trends in Fig. 2.17(d) are contained in Eq. (2.55). Here, we focus on the  $\chi \rightarrow 0$  ( $m \rightarrow 0$ ) limit, which allows us to establish  $(\Delta\epsilon_{xc}/\Delta k_t) = 4.0$  for  $\chi \rightarrow 0$ .

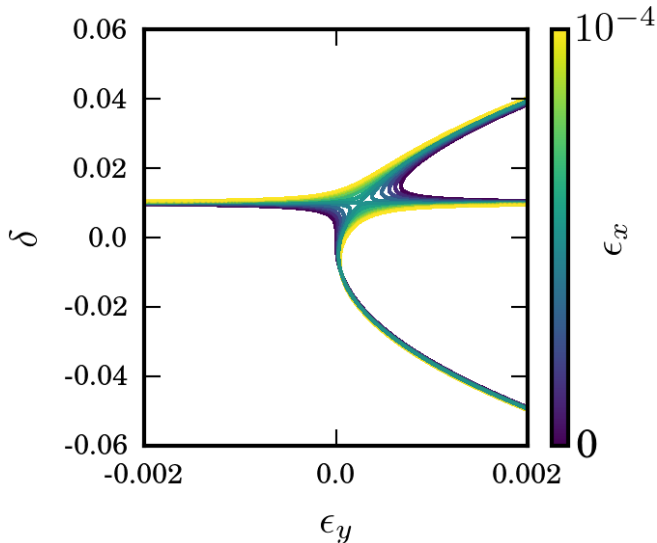


**Figure 2.21:** Based on Eq. (2.58), the unfolding of an imperfect pitchfork bifurcation confirmed for a system with  $\chi \rightarrow 0$  ( $m = 10^{-2}$ ),  $k_l = 0.50$ ,  $k_t = 0.0$  in the  $(\epsilon_y, \delta)$  space and for a series of small values of  $\epsilon_x$ .

## 2.5.2 Perfect Pitchfork Bifurcation

We consider the case for a monoholar system for which the value of the symmetry breaking parameter  $m = 0$ . Substituting  $m = 0$  in Eq. (2.55) leads to:

$$\frac{(\epsilon_x + \epsilon_y - \frac{2k_t}{k_l})}{(\frac{\epsilon_x}{6} + \frac{\epsilon_y}{6} + 1)} \delta - \delta^3 = 0. \quad (2.59)$$

Clearly, the above equation resembles the normal form of the pitchfork bifurcation given by Eq. (2.56). Let us assume  $(\epsilon_x + \epsilon_y - \frac{2k_t}{k_l}) / (\frac{\epsilon_x}{6} + \frac{\epsilon_y}{6} + 1) = \mu$ . The critical points then become:

$$\delta_1 = 0, \quad \delta_2 = \sqrt{\mu}, \quad \delta_3 = -\sqrt{\mu}. \quad (2.60)$$

These three solution branches intersect at the bifurcation point  $\mu = 0$  (i.e.  $\epsilon_x + \epsilon_y = 2k_t/k_l$ ),  $\delta = 0$ . We can rewrite Eq. 2.59 as:

$$f(\delta, \mu) = \mu\delta - \delta^3 = 0. \quad (2.61)$$

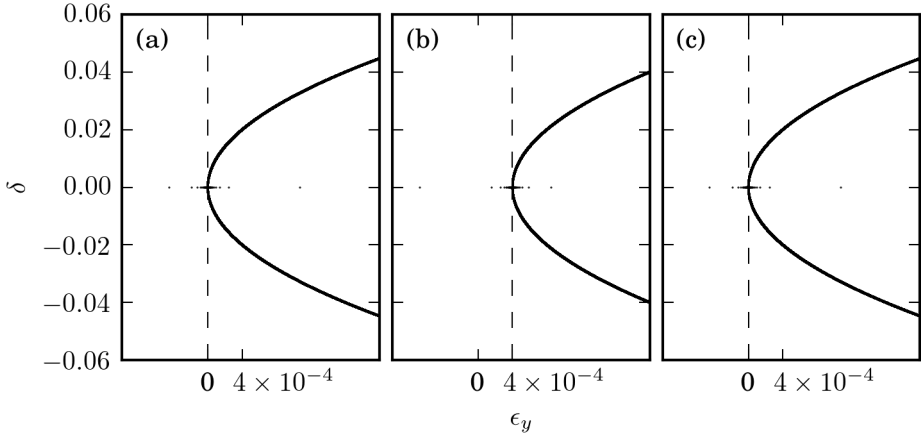


**Figure 2.22:** Pitchfork bifurcations diagrams for a monoholar system with symmetry breaking parameter  $m = 0$  in  $(\epsilon_y, \delta)$  phase space (based on Eq. 2.59),  $k_l = 0.50$  and for specific values of  $\epsilon_x$  and  $k_t$ . (a)  $\epsilon_x = 0.0, k_t = 0.0$ .  $\epsilon_y = 0.0, \delta = 0.0$  is the bifurcation point. (b)  $\epsilon_x = 0.0, k_t = 10^{-4}$ . The bifurcation point shifts horizontally towards the right at  $\epsilon_y = 4 \times 10^{-4}$ . (c)  $\epsilon_x = 4 \times 10^{-4}, k_t = 10^{-4}$  brings the bifurcation point back at  $\epsilon_y = 0.0, \delta = 0.0$ .

Thus,

$$f_\delta(\delta_1, \mu) = \mu, \quad f_\delta(\delta_{(2,3)}, \mu) = -2\mu. \quad (2.62)$$

Therefore, the solution branch  $\delta_1$  is stable if  $\mu < 0$ , whereas the branches  $\delta_2$  and  $\delta_3$  are stable if  $\mu > 0$ .  $\delta_1$  and  $\delta_{2,3}$  have opposite stability and exchange stability at  $\mu = 0, \delta = 0$ . We use Eq. 2.59 to construct bifurcation diagrams for a monoholar system in the phase space  $(\epsilon_y, \delta)$  for specific values of  $\epsilon_x$  and  $k_t$ . We keep  $k_l$  fixed at 0.50. Fig. 2.22(a) shows the bifurcation diagram for  $\epsilon_x = 0, k_t = 0$ . We have a perfect pitchfork bifurcation with  $\epsilon_y = 0, \delta = 0$  being the bifurcation point. From an experimental point of view, the monoholar sheet with negligible bending stiffness of the interhole ligaments buckles right at the application of the vertical strain. Fig. 2.22(b) shows the diagram for  $\epsilon_x = 0, k_t = 10^{-4}$ . We notice a horizontal shift towards right in the bifurcation diagram. The new bifurcation point is now at  $\epsilon_y = 4 \times 10^{-4}, \delta = 0$ , which is where  $\mu$  takes on the value zero. Hence, in our model, a monoholar sheet with a finite stiffness of the interhole ligaments

initially undergoes an elastic compression before undergoing buckling and the subsequent pattern transformation. Finally, keeping  $k_t = 10^{-4}$ , we change the value of  $\epsilon_x$  to  $4 \times 10^{-4}$  - the bifurcation diagram shifts to the left, thus retaining  $\epsilon_y = 0, \delta = 0$  as the bifurcation point - a finite critical value of  $\epsilon_x$  tightly compresses the horizontal ligaments, whose buckling occurs right at the onset of the vertical strain.

We draw a couple of important conclusions based on Eq. (2.59): *(i)*  $\epsilon_x$  and  $\epsilon_y$  are interchangeable and play similar roles for a symmetrical monoholar system, and *(ii)* from the point of view of confinement controlled experiments, it can be seen that if  $\epsilon_x = 2k_t/k_l$ , the system is at the bifurcation point. We have also shown this diagrammatically through Fig. 2.22. We use this observation to justify the scaling of  $\epsilon_{xc}$  with  $k_t$  for systems with  $\chi \rightarrow 0$  [Fig. 2.17(a)]. We notice that for  $k_l = 0.50$ , the critical value of  $\epsilon_x$  required to set the system at the bifurcation point scales linearly with slope 4. Hence, we rationalize the numerical observation shown in Fig. 2.17(a).

## 2.6 Conclusions

We have shown that the physics of confined quasi-2D mechanical metamaterials can be captured by a seemingly simple mechanisms of rotating polygons. As a particular example, we demonstrated that a spring-coupled mechanism consisting of pin-jointed rectangles, called the soft mechanism (§2.2), is able to fully model the experimentally observed complex mechanical behavior (regimes *(i)* – *(iv)*) of a confined biholar sheet [20].

We then understood the transition from one regime to another and the involved bifurcations from solely a geometrical perspective, and outlined a generic strategy to rationally design the mechanical metamaterials with the desired confinement controlled response. To model a more realistic scenario, we coupled the hinges of the soft mechanism with torsional springs. We found out that this leads to an increase in the values of  $\epsilon_{xc}$ , the critical strain values at which the regime transitions occur. Finally, we explored the soft mechanism for the limiting case where  $\chi \rightarrow 0$ . We demonstrate that, near this singularity, the different mechanical regimes emerge from the unfolding of an imperfect pitchfork bifurcation.

## Acknowledgments

The work presented in this chapter is part of an industrial partnership programme (IPP) ‘*Computational Sciences for Energy Research (CSER)*’ started in 2012, and funded by the Shell Global Solutions International B.V., the Netherlands Organization for Scientific Research (NWO) and the Foundation for Fundamental Research on Matter (FOM).

